

AD-A034 537

ARNOLD ENGINEERING DEVELOPMENT CENTER ARNOLD AIR FORC--ETC F/G 20/4
AN INVESTIGATION OF DUCTED, TWO-STREAM, VARIABLE-DENSITY, TURBU--ETC(U)
JAN 77 R J SCHULZ

UNCLASSIFIED

AEDC-TR-76-152

AFOSR-TR-76-1087

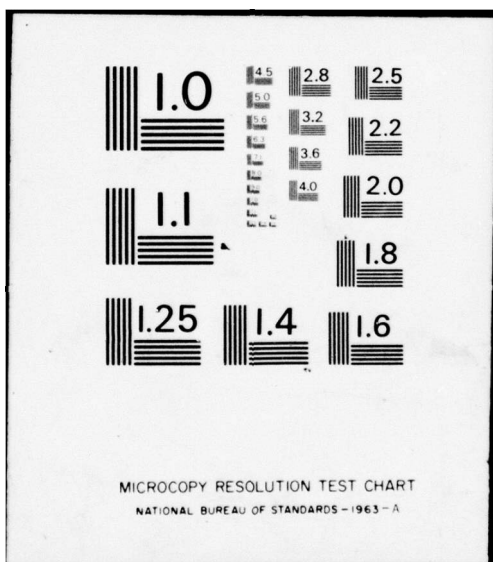
NL

| OF |
AD
A034537



END

DATE
FILMED
2-77



MICROCOPY RESOLUTION TEST CHART
NATIONAL BUREAU OF STANDARDS - 1963 - A

ADA 034537



AEDC-TR-76-152
AFOSR-TR-76-1087

12

PL.

AN INVESTIGATION OF DUCTED, TWO-STREAM,
VARIABLE-DENSITY, TURBULENT JET MIXING
WITH RECIRCULATION

ENGINE TEST FACILITY
ARNOLD ENGINEERING DEVELOPMENT CENTER
AIR FORCE SYSTEMS COMMAND
ARNOLD AIR FORCE STATION, TENNESSEE 373899

January 1977

Final Report for Period May 23, 1975 – June 30, 1976

Approved for public release; distribution unlimited.

Prepared for

AIR FORCE OFFICE OF SCIENTIFIC RESEARCH
BOLLING AIR FORCE BASE
WASHINGTON, D. C. 20332

DDC-R
JAN 1977
REF ID: A64116

NOTICES

When U. S. Government drawings specifications, or other data are used for any purpose other than a definitely related Government procurement operation, the Government thereby incurs no responsibility nor any obligation whatsoever, and the fact that the Government may have formulated, furnished, or in any way supplied the said drawings, specifications, or other data, is not to be regarded by implication or otherwise, or in any manner licensing the holder or any other person or corporation, or conveying any rights or permission to manufacture, use, or sell any patented invention that may in any way be related thereto.

Qualified users may obtain copies of this report from the Defense Documentation Center.

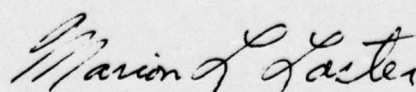
References to named commercial products in this report are not to be considered in any sense as an endorsement of the product by the United States Air Force or the Government.

This report has been reviewed by the Information Office (OI) and is releasable to the National Technical Information Service (NTIS). At NTIS, it will be available to the general public, including foreign nations.

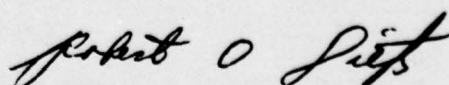
APPROVAL STATEMENT

This technical report has been reviewed and is approved for publication.

FOR THE COMMANDER



MARION L. LASTER
Research & Development
Division
Directorate of Technology



ROBERT O. DIETZ
Director of Technology

UNCLASSIFIED

14 REPORT DOCUMENTATION PAGE		READ INSTRUCTIONS BEFORE COMPLETING FORM	
REPORT NUMBER AEDC-TR-76-152 / AFOSR-TR-76-1087	2. GOVT ACCESSION NO. 15	3. RECIPIENT'S CATALOG NUMBER 16	
TITLE (Type or subtitle) AN INVESTIGATION OF DUCTED, TWO-STREAM, VARIABLE-DENSITY, TURBULENT JET MIXING WITH RECIRCULATION.		5. TYPE OF REPORT & PERIOD COVERED Final Report - May 23, 1975 - June 30, 1976	
7. AUTHOR(s) 10 Roy J. Schulz ARO, Inc.		6. PERFORMING ORG. REPORT NUMBER 23 May 75-30 Jun	
9. PERFORMING ORGANIZATION NAME AND ADDRESS Arnold Engineering Development Center (DY) Air Force Systems Command Arnold Air Force Station, Tennessee 37389		10. PROGRAM ELEMENT, PROJECT, TASK AREA & WORK UNIT NUMBERS Program Elements 61102 and 65807F	
11. CONTROLLING OFFICE NAME AND ADDRESS Arnold Engineering Development Center (DYFS) Arnold Air Force Station Tennessee 37389		12. REPORT DATE 11 Jan 77	
14. MONITORING AGENCY NAME & ADDRESS (If different from Controlling Office) 16 Approved for public release; distribution unlimited.		13. NUMBER OF PAGES 86	
15. SECURITY CLASS. (of this report) UNCLASSIFIED		15a. DECLASSIFICATION/DOWNGRADING SCHEDULE N/A	
16. DISTRIBUTION STATEMENT (of this Report) 18 AFOSR		17. DISTRIBUTION STATEMENT (of the report entered in Block 16, if different from Report) 19 TR-76-1087	
18. SUPPLEMENTARY NOTES Available in DDC			
19. KEY WORDS (Continue on reverse side if necessary and identify by block number) jet mixing flow mathematical analysis gas flow experimental data recirculation theory turbulent mixing			
20. ABSTRACT (Continue on reverse side if necessary and identify by block number) An investigation was conducted of two-stream, variable-density, turbulent jet mixing with recirculation confined within an axisymmetric duct that simulated a combustor configuration. The recirculating flow fields in the combustor simulator were the result of coaxial jet mixing between a central, primary air stream with a velocity of about 650 ft/sec and an annular secondary stream of hydrogen with velocities of 13, 23, or 48 ft/sec, depending on the desired test conditions. Experimental measurements are presented			

DD FORM 1 JAN 73 1473 EDITION OF 1 NOV 65 IS OBSOLETE

→ next
page

UNCLASSIFIED

042550

48

UNCLASSIFIED

20. ABSTRACT (Continued)

of radial distributions of time-averaged axial velocity and hydrogen mass fraction, axial distributions of time-averaged static pressure on the duct wall, axial velocity on the duct centerline, and hydrogen mass fraction on the duct wall and on the duct centerline. A theoretical study of the experimental flows was also conducted using a finite difference numerical solution technique as reported by Gosman, et al. for the calculation of viscous, recirculating flows. A simple Prandtl-type eddy viscosity model was selected to represent the turbulent transport processes. Comparison of theory and experiment shows that the predictive technique and the turbulence transport model require further development before accurate prediction of recirculating turbulent flows can be realized.



PREFACE

The work reported herein was conducted by the Arnold Engineering Development Center (AEDC), Air Force Systems Command (AFSC), under the sponsorship of the Air Force Office of Scientific Research (AFOSR) under Program Elements 61102F and 65807F. The results were obtained by ARO, Inc. (a subsidiary of The Sverdrup Corporation), contract operator of AEDC, AFSC, Arnold Air Force Station, Tennessee. The work was performed under ARO Project Numbers R33P-93A and R33P-59A. The author of the report was Roy J. Schulz, ARO, Inc. The manuscript (ARO Control Number ARO-ETF-TR-76-80) was submitted for publication on July 23, 1976.



CONTENTS

	<u>Page</u>
1.0 INTRODUCTION	
1.1 Description of the Problem	7
1.2 Survey of the Literature	9
2.0 THEORETICAL ANALYSIS	
2.1 Introduction	14
2.2 Numerical Solution Technique	16
2.3 Boundary Conditions	19
2.4 Practical Difficulties Arising in the Application of the Special Code	19
2.5 Turbulence Transport Model	25
3.0 APPARATUS	
3.1 Test Cell	27
3.2 Instrumentation	28
3.3 Test Procedure	29
3.4 Determination of the Primary Jet Nozzle Flow Characteristics	31
3.5 Precision of Measurements	31
4.0 RESULTS AND DISCUSSION	
4.1 Introduction	32
4.2 Comparison of Experimental and Theoretical Profiles of Axial Velocity	33
4.3 Comparison of Experimental and Theoretical Radial Profiles of Hydrogen Mass Fraction	34
4.4 Comparison of Experimental and Theoretical Axial Distributions of Axial Velocity on the Centerline	35
4.5 Comparison of Experimental and Theoretical Axial Distributions of Hydrogen Mass Fraction on the Wall and on the Centerline	36

<u>Figure</u>	<u>Page</u>
4.6 Comparison of Experimental and Theoretical Axial Distributions of Static Pressure along the Wall	37
4.7 Comparison of Experimental and Theoretical Axial Locations of Stagnation Points on the Wall	37
5.0 CONCLUSIONS	40
REFERENCES	42

ILLUSTRATIONS

1. Schematic of Turbulent Ducted Mixing with Recirculation	47
2. Configuration of the Computational Mesh and the Boundaries of the Region Encompassing the Recirculating Flows	48
3. Eddy Viscosity Distribution for Confined Recirculating Flows which Includes Potential Flow Regions	49
4. Recirculating Flow Combustor Simulator Facility	50
5. Primary Flow Nozzle Assembly	51
6. Pitot Pressure and Gas Sample Probe	52
7. Primary Jet Exit Velocity Profiles Compared with Turbulent Pipe Flow Profile at the Same Reynolds Number, $N_{Re_D} = 10^5$	53
8. Comparison of Experimental and Theoretical Radial Distributions of Mean Axial Velocity	54
9. Comparison of Experimental and Theoretical Radial Distributions of Mean Hydrogen Mass Fraction	58
10. Comparison of Experimental and Theoretical Axial Distributions of Nondimensionalized Mean Axial Velocity on the Centerline of the Combustor Simulator	62

<u>Figure</u>	<u>Page</u>
11. Comparison of Experimental and Theoretical Axial Distributions of Hydrogen Mass Fraction at the Wall and Centerline	64
12. Comparison of Experimental and Theoretical Axial Distributions of Wall Static Pressure	67
13. Estimated Locations of Points of Zero Mean Axial Velocity	69
14. Comparison of Theoretical and Experimental Wall Stagnation Point Location	70
15. Axial Locations of Forward and Rear Stagnation Points in Recirculating Combustor Flows for Constant and Variable Density Jet Mixing as Functions of the Craya-Curtet Number	71

TABLES

1. Coefficients of the Conservation Equation (Eq. (12)) . . .	72
2. Source Terms of the Conservation Equations	72
3. Uncertainties in Measured and Calculated Parameters (ϕ)	73
4. Hydrogen-Air Mixing Experimental Test Conditions	74

APPENDIX

A. Experimental Data	75
NOMENCLATURE	82

1.0 INTRODUCTION

1.1 DESCRIPTION OF THE PROBLEM

The results of an experimental and theoretical investigation of the recirculating flow fields induced by ducted, variable-density, turbulent jet mixing are presented. Recirculating flow fields established by turbulent jet mixing of two coaxial streams in a constant-area, axisymmetric duct occur in many industrial and aerospace burner, furnace, or combustor configurations. The so-called "sudden-expansion" or "dump" combustors used in ramjet-rocket propulsion systems are designed on the principle of establishing and maintaining combustion in regions of recirculating flow within the combustors.

Figure 1 shows the essential features of the type of recirculating flow field studied herein. For a certain range of fluid influx conditions, ducted jet mixing of coaxial streams leads to the creation of an eddy of recirculating fluid, existing on a time-averaged basis as a toroidal, highly vortical region with high levels of turbulent intensities and relatively low average velocities. The eddy of the recirculating region is generated when the "entrainment capacity" of the higher velocity primary jet stream is not satisfied by the weight flow of the outer, lower velocity secondary stream. For those conditions, the primary jet "establishes" the recirculation eddy which serves to feed mass into the jet thus dissipating the jet mechanical energy.

In all essential time-averaged features, this recirculating flow is a stationary, separated, turbulent, toroidally shaped region with an eddy-like structure wherein back-flowing currents carry mass, energy, and momentum from downstream toward the inlet station. The recirculation eddy can exist with or without secondary flow. However, at a secondary flow rate equal to or greater than a critical

"blow-off" value, the recirculation eddy structure cannot form, and the duct flow will be characterized everywhere by positive axial velocity components. The pertinent features of the flow field with recirculation are:

1. The axial location of the two points on the duct wall, denoted X_{FS} and X_{RS} in Fig. 1, which are characteristic time-averaged stagnation points of the flow,
2. The time-averaged axial velocity field,
3. The time-averaged distribution of mass, energy or temperature of the fluid from the primary flow which characterizes the qualitative and quantitative nature of the mixing that has occurred between the two streams, and
4. The time-averaged axial distribution of wall static pressure.

All of these gross features of the flow, their spatial distributions and magnitudes, appear from experimental evidence to be dependent upon the ratios (u_{s_o}/u_p , ρ_s/ρ_p , R_s/R_p), the Reynolds number based on the primary flow at the nozzle exit station (N_{Re_p}), and upon chemical reactions, if any, occurring in the flow. However, it is also an empirical observation that, for values of the primary jet Reynolds number defined by

$$N_{Re_p} = \frac{\rho_p u_p R_p}{\mu_p} \quad (1)$$

greater than about 1.5×10^4 , the time-averaged velocity, species concentration, and static-pressure fields become independent of the jet Reynolds number (N_{Re_p}); this condition is satisfied in the present study. In the present investigation, the flow fields studied were nonreactive, hence of uniform total temperature. However, density variations were created throughout the flow fields by the mixing of jets of different molecular weight.

The principal objective of the present study was to obtain time-average flow field data in sufficient detail to define the recirculating flow fields that develop from ducted, non-reactive but variable-density, axisymmetric, turbulent jet mixing. The density variations were achieved by utilizing air as the primary stream fluid and hydrogen as the secondary stream fluid. The data obtained were spatial distributions of time-average velocity, hydrogen mass fraction, and wall static pressure for three sets of primary and secondary stream influx conditions. The data may be used for preliminary design estimates for combustors, or combustor processes, and to develop and evaluate theoretical models or predictive techniques for such flows and processes.

In the present study, the data obtained were compared with theoretical predictions made by using a slightly modified version of the theoretical model and numerical solution procedure developed by Gosman, et al., (Ref. 1). The theoretical solutions were calculated based on a simple Prandtl-type eddy viscosity model of the turbulent transport processes.

1.2 SURVEY OF THE LITERATURE

Thring and Newby (Ref. 2) were concerned with analyzing the operating conditions within an oil-fired, recirculating-flow burner. The principal objective of their analysis was "... to employ an

isothermal constant density mixing model to predict approximately the position of a stoichiometric contour in a hot flame burning fluid atomized oil." The importance of the paper by Thring and Newby was that it presented evidence that, when $R_s/R_p \geq 10$, the jet mixing processes in combustors could be interpreted qualitatively like free turbulent jet mixing and that they identified a parameter that "correlated" combustor mixing processes with variations in the ratios of the weight flows and radii of the primary stream to the secondary stream.

Curtet (Ref. 3) presented an analysis of ducted, turbulent jet mixing processes which was developed by himself and A. Craya based on solving the boundary layer forms of the Navier-Stokes equations using an integral technique. In order to obtain solutions, Curtet assumed that the confined jet mixing processes could be based on empiricisms developed by analysis of free turbulent jet mixing processes. Curtet showed that this type of analysis, an integral analysis, could predict certain features of the process of confined jet mixing with recirculation, for example, the amount of material in the recirculation eddy, over appropriate ranges of characteristic parameters of the system, such as, u_{s_0} , u_p , R_s , and R_p . The analysis by Craya and Curtet was developed specifically for constant density, isothermal, confined, turbulent jet mixing. Curtet, like Thring and Newby, reported a mixing similitude parameter that would serve to correlate the gross structural features of the flow fields as they varied with changing primary and secondary stream influx conditions.

To supplement the theoretical study, Curtet presented the results of an experimental investigation of recirculating flow in a combustor configuration. The experimental investigation covered recirculating flows in both planar and axisymmetric combustor configurations. The data were obtained from experiments based on isothermal, constant density, confined, turbulent jet mixing but unfortunately, the data

may be dependent on the exit geometry of the combustor that was used in the experiments and thus may lack generality.

On the other hand, papers providing detailed data on confined jet mixing with recirculation that do not depend on downstream or exit conditions were prepared and presented by Becker, Hottel, and Williams (Refs. 4, 5, and 6). The papers presented data which define the wall static pressure, concentration, and velocity fields which result from constant density, isothermal, confined jet mixing processes with recirculation. The data also serve to define the intermittent, or "turbulent," nature of this class of flows because Becker, Hottel, and Williams presented spatial distribution of intermittency and concentration fluctuation intensities that existed in their recirculating combustor flows. Becker, Hottel, and Williams proposed yet another parameter (C_T) to serve as a parameter for the correlation of the gross flow field properties with variations in primary-to-secondary stream velocity and radius ratios. Their definition of C_T , which they named the Craya-Curtet parameter (Ref. 4), is

$$C_T = \frac{u_k}{\frac{\pi}{u_o}} \quad (2)$$

where

$$u_k = \frac{1}{R_s^2} [u_p R_p^2 + u_{s_o} (R_s^2 - R_p^2)] \quad (3)$$

and

$$u_o^* = \left[\frac{1}{R_s^2} [u_p^2 R_p^2 + u_{s_o}^2 (\frac{R_s^2}{2} - R_p^2)] - \frac{1}{2} u_k^2 \right]^{\frac{1}{2}} \quad (4)$$

The form of C_T given above is based on uniform parallel influx or entrance conditions of the primary and secondary streams when they are separated by a thin nozzle lip. Details and analysis of the Becker, Hottel, and Williams experiments are provided in Ref. 7.

Barchilon and Curtet (Ref. 8) also presented experimental data defining the flow fields developing from isothermal, constant density, confined, axisymmetric, turbulent jet mixing with recirculation. Their data defined time-averaged axial velocity fields, wall static pressure distributions, and turbulent velocity fluctuation intensity distributions. Barchilon and Curtet also compared and correlated the spatial variations of the gross flow field characteristics, such as the structure of the recirculating eddy, with the values of the Craya-Curtet parameter (C_T). Their study was carried out with both gaseous and liquid streams as the experimental fluids.

Other papers have been written about recirculating combustor flows, but these papers are not sufficiently useful to warrant discussion in the present study. At present, it is more important to consider the differences and similarities in the data presented by Becker, Hottel, and Williams and by Barchilon and Curtet since their papers contain the principal data which define ducted jet mixing with recirculation under isothermal, constant density conditions. In both cases, experiments were conducted in duct geometries where the duct-to-primary jet radius was relatively large ($R_s/R_p \geq 10$) so that, to a fair approximation, the jet mixing processes exhibit qualitative and quantitative features similar to free turbulent jet mixing processes. Both set of experiments were concerned with the investigation of constant density, isothermal, axisymmetric, ducted turbulent jet mixing with recirculation wherein both primary and secondary streams enter the mixing region with uniform velocity profiles. Both sets of experiments provided data defining the time-averaged axial velocity fields, wall static pressure distributions, and distributions of quantities that characterize the fluctuations of properties of the flow fields in an attempt to characterize the "turbulent" nature of the flows. In both cases, the characteristic features of the flow fields, such as the axial locations of the forward and rear stagnation points, were correlated with C_T . The similitude parameter was varied over a wide range, including conditions

resulting in blow-off of the recirculation zone. Barchilon and Curtet showed that the instantaneous structure of recirculating flows is not regular, that is, not characterized by a single eddy. Rather the recirculation region is characterized by one or more short-lived eddies and extremely high fluctuating velocities (relative to local or mean velocities), such that large-scale turbulent motions exist over random time scales. Becker, Hottel, and Williams showed that integral length scales or standard deviations of turbulent fluctuations of flow properties in jet mixing flows with recirculation vary both radially and longitudinally throughout the flows. Moreover, it was shown that these measures of turbulent fluctuation, such as the standard deviation of the axial intermitting profiles, could be the same order of magnitude as the duct radius.

On the other hand, an analysis and evaluation of the sets of data presented by Becker, Hottel, and Williams and by Barchilon and Curtet (Ref. 7) demonstrated both qualitative and quantitative differences between sets of data for conditions that were supposedly equivalent, based on correlations with C_T . For example, while the upstream edge of the recirculation eddy (X_{FS}) appeared to correlate with C_T , behaving approximately the same in both sets of experiments, the data defining the behavior or correlation of the downstream stagnation point location (X_{RS}) with C_T was substantially different in the two sets of experiments. Also, the rates of decay of axial velocity on the centerline of the ducts differs qualitatively between the two sets of experiments for turbulent mixing conditions that are supposedly equivalent, based on correlations with C_T . Therefore, it is clear that additional experiments are required to determine if mixing similitude parameters such as the Craya-Curtet parameter, are suitable for expressing the equivalency of confined, turbulent flows. Also, the data presented by Becker, Hottel, and Williams and by Barchilon and Curtet which illustrate the "turbulent" nature of recirculating flow fields must be verified and extended by future research on such flows.

In practical applications, the flows in most recirculating flow combustors are established by variable density turbulent jet mixing. The density variations usually result from the mixing of primary and secondary streams of different temperatures, molecular weights, or from exothermic chemical reactions occurring in the mixing process. There are, apparently, no experimental data defining variable density, confined, turbulent jet mixing with recirculation which exist in sufficient detail to be useful for engineering design purposes or for the development and evaluation of theoretical predictive techniques for combustor design. Of immediate interest is the mean velocity, concentration, and wall static pressure field-definition for recirculating combustor flows wherein large density gradients initially exist across the jet mixing layers. Experiments may be either reactive or nonreactive, but the relative simplicity of nonreactive to reactive experiments strongly implied that nonreactive experiments be conducted first. Therefore, a primary purpose of the present study was to provide a "first-cut" set of data defining the flow fields of variable density, nonreactive, ducted, axisymmetric turbulent jet mixing with recirculation where the density variations were caused by the mixing of two streams of greatly different molecular weight.

2.0 THEORETICAL ANALYSIS

2.1 INTRODUCTION

The special code for combustor problems developed and reported by Gosman, et al. (Ref. 1), was designed to predict the flow fields within general axisymmetric combustor configurations. The code, called hereafter simply the special code, was applied in the present investigation together with an assumed model for the turbulent or effective viscosity to make theoretical predictions of the variable-density, combustor-type, recirculating flow fields experimentally investigated in the present study.

A set of governing equations of motion for viscous, axisymmetric, recirculating flows was derived from the Navier-Stokes equations, the species conservation equation, and an identity relating stream function and vorticity by Gosman, et al. The equations are, respectively,

$$\begin{aligned} r^2 \left[\frac{\partial}{\partial x} (\omega \frac{\partial \psi}{\partial r}) - \frac{\partial}{\partial r} (\omega \frac{\partial \psi}{\partial x}) \right] - \frac{\partial}{\partial x} [r^3 \frac{\partial}{\partial x} (\mu_E \omega)] \\ - \frac{\partial}{\partial r} [r^3 \frac{\partial}{\partial r} (\mu_E \omega)] + r d_\omega = 0 \end{aligned} \quad (5)$$

$$\frac{\partial}{\partial x} (\tilde{C} \frac{\partial \psi}{\partial r}) - \frac{\partial}{\partial r} (\tilde{C} \frac{\partial \psi}{\partial x}) - \frac{\partial}{\partial x} (\rho D_{\tilde{C}_E} r \frac{\partial \tilde{C}}{\partial x}) - \frac{\partial}{\partial r} (\rho D_{\tilde{C}_E} r \frac{\partial \tilde{C}}{\partial r}) + r S_{\tilde{C}} = 0 \quad (6)$$

$$\frac{\partial}{\partial x} \left(\frac{1}{\rho r} \frac{\partial \psi}{\partial x} \right) + \frac{\partial}{\partial r} \left(\frac{1}{\rho r} \frac{\partial \psi}{\partial r} \right) + r \omega = 0 \quad (7)$$

The variable (ψ) is the stream function, defined by the set of equations

$$\frac{\partial \psi}{\partial x} = - \rho v r \quad (8)$$

and

$$\frac{\partial \psi}{\partial r} = \rho u r \quad (9)$$

The variable (ω) is the vorticity divided by the radius, that is,

$$\omega = \Omega / r \quad (10)$$

where vorticity was written, as

$$\Omega = \frac{\partial v}{\partial x} - \frac{\partial u}{\partial r} \quad (11)$$

The variable (\tilde{C}) represents any scalar, "transportable, conserved" quantity. For example, in the present investigation, it represents the mass fraction of the secondary stream fluid which is gaseous hydrogen.

The governing equations are a set of coupled, elliptic, partial differential equations. Therefore, solution can be obtained only if boundary conditions for ψ , ω , and \tilde{C} are prescribed over the entire boundary enveloping the flow field.

2.2 NUMERICAL SOLUTION TECHNIQUE

A method of solving the set of governing equations was developed and presented by Gosman, et al. (Ref. 1). They cast the set of governing equations into a common format, specifically, writing each equation in the form

$$a_\phi \left[\frac{\partial}{\partial x} \left(\phi \frac{\partial \psi}{\partial r} \right) - \frac{\partial}{\partial r} \left(\phi \frac{\partial \psi}{\partial x} \right) \right] - \frac{\partial}{\partial x} [b_\phi r \frac{\partial}{\partial x} (c_\phi \phi)] - \frac{\partial}{\partial r} [b_\phi r \frac{\partial}{\partial r} (c_\phi \phi)] + r d_\phi = 0 \quad (12)$$

where ϕ represents ψ , ω , or \tilde{C} . The necessary and corresponding set of coefficients (a_ϕ , b_ϕ , and c_ϕ) are those shown in Table 1 opposite their appropriate functions (ϕ). The terms (d_ϕ) are the corresponding source terms for the ϕ and are given in Table 2 opposite their corresponding functions (ϕ).

The source term for ω contains a function (S_ω) given by

$$S_\omega = \frac{2}{r} [\text{grad}(\hat{i}_x \cdot \vec{V}) \cdot \text{iso}(\hat{i}_x \cdot \text{grad } \mu_E) + \text{grad}(\hat{i}_r \cdot \vec{V}) \cdot \text{iso}(\hat{i}_r \cdot \text{grad } \mu_E) - \text{iso}(\text{div } \vec{V}) \cdot \text{grad } \mu_E] \quad (13)$$

where \hat{i}_x and \hat{i}_r are unit vectors in the x and r direction, respectively, and where, given the dummy variables (A and \vec{A})

$$\text{grad } A = \frac{\partial A}{\partial x} \hat{i}_x + \frac{\partial A}{\partial r} \hat{i}_r \quad (14)$$

$$\text{iso } A = - \frac{\partial A}{\partial r} \hat{i}_x + \frac{\partial A}{\partial x} \hat{i}_r \quad (15)$$

and

$$\text{div } \vec{A} = \frac{1}{r} [r \frac{\partial A_x}{\partial x} + \frac{\partial}{\partial r}(r A_r)] \quad (16)$$

in cylindrical polar coordinates for axisymmetric systems.

Therefore, S_ω in an expanded format becomes

$$S_\omega = \frac{2}{r} [\frac{\partial^2 \mu_E}{\partial x \partial r} (\frac{\partial v}{\partial r} - \frac{\partial u}{\partial x}) + \frac{\partial^2 \mu_E}{\partial x^2} \frac{\partial u}{\partial r} - \frac{\partial^2 \mu_E}{\partial r^2} \frac{\partial v}{\partial x} + \frac{\partial \mu_E}{\partial x} (\frac{\partial}{\partial r} (\frac{\partial u}{\partial x} + \frac{v}{r} + \frac{\partial v}{\partial r})) - \frac{\partial \mu_E}{\partial r} (\frac{\partial}{\partial x} (\frac{\partial u}{\partial x} + \frac{v}{r} + \frac{\partial v}{\partial r}))] \quad (17)$$

Gosman, et al., argue that S_w contributes negligibly to the total vorticity source term (d_w) and may be neglected. Certainly, this is true for constant viscosity flows. In the present study, S_w was presumed to be negligible despite the fact that considerable viscosity gradients existed in the fields of the numerical solution because of the turbulence transport model used in the present study.

Gosman, et al., presented a technique for obtaining a set of finite-difference equations analogous to and derived from Eq. (12). The ultimate result of their analysis is a set of coupled, algebraic equations called successive substitution equations or formulas. One such equation exists for each dependent variable (ϕ). The method of solving for the values of ϕ in the interior of the computational region is to apply the successive substitution formula alternately, in complete sweeps of the computational field, in a point by point manner for each ϕ . The stability of the computational procedure is obtained for flows characterized by large (greater than two) Reynolds numbers that are based on computational cell spacing, by (1) the use of an "up-wind" differencing technique for establishing finite difference expressions of convective flux terms of Eq. (12), (2) by requiring that certain coefficients in the successive substitution formula be bounded in their individual and collective numerical values; and, finally (3) by an appropriate use of under- or over-relaxation techniques. In the present study, no systematic investigation or use of under- or over-relaxation factors was attempted. The under- or over-relaxation factors that were used ranged from 0.9 to 1.1.

In addition, in the course of the present study, the numerical solutions of the flow field were accepted as being converged when the maximum variations in the axial distribution of centerline axial velocity ceased to change by more than one percent with successive iterations of the flow field.

2.3 BOUNDARY CONDITIONS

Techniques for the establishment of boundary conditions for the dependent variables (ψ , ω , and \tilde{C}) are provided by Gosman, et al. In general, at the solid walls, the value of ω and the gradients of ω are prescribed such that axial and radial velocity components are zero. At the plane of the primary jet nozzle exit, the boundary conditions on ψ and ω are such that they define uniform, parallel primary and secondary flow influx conditions everywhere except at the nozzle lip. Along the axis of symmetry, the special code establishes the axis value of ω as a linear extrapolation of the values of ω at one and two radially adjacent nodes. At the outlet plane, the axial gradients of ψ and ω are set to zero. For the conserved, transportable scalar quantity (\tilde{C}) the boundary condition on the wall and on the axis of symmetry is

$$\partial \tilde{C} / \partial r = 0 \quad (18)$$

At the plane of the primary nozzle exit, \tilde{C} is constant across the primary and secondary stream, equal to 0.0 and 1.0, respectively. Finally at the outlet plane, the boundary conditions are such that

$$\partial \tilde{C} / \partial x = 0 \quad (19)$$

2.4 PRACTICAL DIFFICULTIES ARISING IN THE APPLICATION OF THE SPECIAL CODE

Four major problems arose in the application of the special code to predict the turbulent, recirculating flows considered in the present study:

1. The specification of vorticity at a nozzle lip,

2. The prediction of static pressure fields,
3. The numerical problems that arise when making computations by utilizing highly stretched or nonuniform mesh configurations, and
4. The problem of obtaining converged solutions for flows with large density gradients in the fields.

Specific approaches have been taken to resolve the difficulties. The approaches which are summarized below are presented in detail in Ref. 7.

2.4.1 Boundary Condition for Vorticity at a Protruding Corner

Gosman, et al., gave techniques and methodology for establishing or defining boundary values for the dependent variables. However, it was found (Ref. 7) that the vorticity at the lip of the primary nozzle was one of the principal parameters that determined the development of the theoretical solution, that is, of the development of the downstream flow field. Gosman, et al., incorporated a special procedure to specify ω at the edges of the nozzle because, as they noted, this point is a point of flow separation from a "protruding corner."

Figure 2 shows the geometry of the boundary of the flows under investigation, and as noted, the points CA and CB, at the edges of the nozzle lip, define the points of flow separation. Many techniques exist for the specification of vorticity at such corners. For example, Roache (Ref. 9) lists seven schemes for assigning values to ω at such corners. Gosman, et al., sets the value of the stream function at the

points CA + 1 and CB + 1 equal to the values of stream function at CA and CB, respectively:

$$\psi_{CA+1} = \psi_{CA} \quad (20)$$

and

$$\psi_{CB+1} = \psi_{CB} \quad (21)$$

Then, the value of the corner vorticity at CA and CB is established through a boundary function that represents the condition

$$u_{CA} = u_{CB} = v_{CA} = v_{CB} = 0 \quad (22)$$

However, the points (CA + 1 and CB + 1) now become effective corner points. The value of the vorticity at these points is established through the following special routine. In principle, Eq. (7) applies, but in reverse,

$$r \cdot \omega = - \left[\frac{\partial}{\partial x} \left(\frac{1}{\rho r} \frac{\partial \psi}{\partial x} \right) + \frac{\partial}{\partial r} \left(\frac{1}{\rho r} \frac{\partial \psi}{\partial r} \right) \right] \quad (23)$$

Therefore, Gosman et al., evaluate this equation numerically and approximately, for example, at CA + 1, by

$$\begin{aligned} \omega_{CA+1} = & - \frac{1}{r_{CA}} [C_{E_\psi} \psi_E + C_{W_\psi} \psi_W + C_{S_\psi} \psi_S + C_{N_\psi} \psi_N \\ & - (C_{E_\psi} + C_{W_\psi} + C_{S_\psi} + C_{N_\psi}) \cdot \psi_{CA}] \end{aligned} \quad (24)$$

where C_{E_ψ} refers to the coefficient of the contribution to the stream function equation (Eq. (7)) from the eastern node (which in the present special routine is CA). The other coefficients have corresponding

meanings. Thus, the "corner" vorticity has been transferred to the first node point downstream at the same radial position. As a result, the jet must issue from the nozzle without expanding or contracting up to the first node point directly downstream of the nozzle lip. But, the mathematical relations thus established by Eqs. (20), (21), and (23) make corner or nozzle lip vorticity dependent on the computational mesh configuration used to simulate the nozzle geometry, the thickness of the simulated nozzle lip, and the x-wise mesh spacing separating such points as CA and CA + 1. Such difficulties have also been noted by other investigators, for example, by Saccia and Kennedy (Ref. 10), without being resolved. Investigation (Ref. 7) has shown, however, that the establishment of a representative corner or lip vorticity is very important and, at present, must be established by trial and error.

Therefore, in the present study, an approach was taken which attempted to relate corner vorticity to the slope of the primary nozzle velocity profile, that is, at the nozzle lip,

$$r\omega_{CA} = \Omega_{CA} = \lambda u_p / R_p \approx -\frac{\partial u}{\partial r} \Big|_{\text{nozzle lip}} \quad (25)$$

Hopefully, therefore, the constant (λ) can be obtained by inspection of the primary flow nozzle exit velocity profiles, which are experimentally determined.

2.4.2 Computation of Static Pressure Fields

The method used in the present study to compute static pressure fields has been applied to both constant density and variable density ducted jet mixing flows with recirculation (Ref. 7). This method is different from the method incorporated in the special code wherein the static pressure field is obtained by integrating the Navier-Stokes equations once the velocity, density, and effective viscosity fields

have been established. Instead, the method used in the present study for constant-area ducted flows was found to be much simpler in procedure and at least as accurate as the method of Gosman, et al. The method is based on two assumptions:

1. Static pressure is constant across the duct, and, hence is a function only of axial distance, and
2. Wall shear stresses contribute negligibly to the sum of pressure area forces and momentum flux in an application of Newton's Second Law to the duct flow.

Under these conditions, the impulse function can be evaluated at any station of the duct, and set equal to its value at the inlet station, that is,

$$F(x) = F(0) \quad (26)$$

where F is the impulse function defined as

$$F(x) = \int_{A(x)} (p + \rho u^2) dA \quad (27)$$

Applying Eq. (6) at the inlet station ($x = 0$) and any other axial station ($x = L$) and equating the expressions yield

$$p(L) + \frac{1}{A(L)} \int_{A(L)} \rho u^2 dA = p(0) + \frac{\rho u_p^2 A_p}{A(L)} + \frac{\rho_s u_{s0}^2 A_s}{A(L)} \quad (28)$$

or

$$p(L) = p(0) + \frac{\rho_p u_p^2 R_p^2}{R_s^2} + \frac{\rho_s u_s^2}{R_s^2} (R_s^2 - R_p^2) - \frac{2}{R_s^2} \int_0^{R_s} \rho u^2 r dr \quad (29)$$

Thus, the pressure at any station of the duct can be found by integration of the profile of ρu^2 at that station in the duct.

2.4.3 Computations Using Nonuniform Mesh Networks

The flow fields to be predicted are formed by turbulent jet mixing between a relatively small diameter, axisymmetric jet and a relatively much larger diameter ducted secondary stream. It was necessary, in order to have reasonable computation times, to carry out the numerical solution in computational mesh networks that were of nonuniform node spacing (Ref. 7). The region near the primary jet nozzle exit plane, called the near field of the jet mixing region, was defined by a mesh network with node spacings which were relatively small compared to the node spacings out near the duct wall and downstream in zones where recirculation was expected to occur. Unfortunately, computations made utilizing highly nonuniform networks of arbitrary construction may result in poor quality solutions (Ref. 7). For example, in computations of nonreactive, multispecies flows, it has been observed (Ref. 7) that the conservation of species criterion may be violated by the solution procedure; the species concentrations at the nodes converge to values which fail to satisfy requirements of global conservation. However, such errors can be lessened by trial-and-error manipulation of the mesh network configuration in which the solution is obtained. The errors can be lessened to the extent that approximate species conservation can be obtained using the solution procedure. For example, mesh configurations were developed (Ref. 7) for the computation of the flows reported by Becker, Hottel, and Williams and for the variable-density flows reported herein.

2.4.4 Obtaining Converged Variable Density Solutions

When attempts were made to compute the hydrogen-air recirculating flows, it was found that the numerical solution procedure would not converge. The difficulty was attributed to numerical instabilities that arose because of the arbitrary initial distributions of the stream function and mixture fraction (or density) that were used to start the calculation procedure. In order to circumvent this problem, the "density dependence" of the stream function was eliminated in the beginning of the iteration process (Ref. 7). To implement this procedure, the stream function variable was modified so that it was explicitly independent of density in the first several hundred iterations of the solution procedure. The net result of the modification was to impose, initially, an incorrect global continuity equation which linked the density field to the field of the modified stream function in a very indirect or weak relationship. This resulted in initially stable numerical solution procedures, albeit with improper governing equations. After 400, or so, iterations an approximately realistic density and velocity field was obtained, and at this point in the solution procedure, integration of the μ field yielded an initial stream function field. This field of density-dependent stream function was sufficiently well posed to allow continued convergence of the solution procedure with the correct governing equations. Details of this method for securing convergence of the solution procedure in variable density computations are outlined in Ref. 7.

2.5 TURBULENCE TRANSPORT MODEL

The closure problem which underlies the overall problem of predicting turbulent flows is that the turbulent transport of momentum, energy, and chemical species must be related to time-averaged flow field quantities or to their gradients. There are several valuable references which present work done to model turbulence transport phenomena for a wide variety of flows, (Refs. 11 through 18). However, comparatively

little work has been performed on turbulence transport modeling in recirculating combustor flows other than the simple observations that the mixing is somewhat like the mixing of free turbulent jets. Therefore, the approach taken in the present study was similar to that proposed in Refs. 3 and 19 and was developed in Ref. 7. Two models for effective viscosity were defined that were based on a Prandtl-type eddy viscosity model for free turbulent jet mixing processes. One model, called the model without potential core, is defined such that

$$\mu_E(x, r) = 0.0285 \rho(x, r) u_p R_p \cdot \frac{x}{X_{core}}, \quad x \leq X_{core} \quad (30)$$

$$\mu_E(x, r) = 0.0285 \rho(x, r) u_p R_p (1 + 0.0036(X - X_{core})/R_p), \quad x > X_{core}$$
(31)

Here, X_{core} represents a length characteristic of a potential core of a free turbulent jet, namely, $X_{core} = 12 R_p$. Note that μ_E is constant across the flow at a given axial station in constant density flow. The second model, called the model with potential core, is defined such that

$$\mu_E(x, r) = 0.0285 \rho(x, r) u_p R_p \cdot \frac{x}{X_{core}}, \quad x \leq X_{core} \quad (32)$$

$$\mu_E(x, r) = 0.0285 \rho(x, r) u_p R_p (1 + 0.0036(X - X_{core})/R_p), \quad x > X_{core}$$
(33)

in the "turbulent" regions of the flow field, and

$$\mu_E(x, r) = \mu_{LAM}(x, r) \quad (34)$$

in the "laminar" regions of the flowfield. The "laminar" and "turbulent" regions of the flow field are defined in Fig. 3. The purpose of the model with potential core was to investigate the importance of accounting for the non-turbulent regions of the recirculating flow (Ref. 7).

Unfortunately, the model with potential core requires more empirical information in its formulation than the model without potential core since the spatial variation of the laminar regions of recirculating flows must be specified.

3.0 APPARATUS

3.1 TEST CELL

To obtain data on variable density mixing with recirculation, specifically the hydrogen-air mixing flows, a combustor simulator was designed and constructed. The combustor design, shown in Fig. 4, consists of a 5-ft steel duct with an inside diameter of 5.24 in. A mechanically driven, axially traversing nozzle assembly, shaped like a cylindrical piston, was mounted inside the duct. The nozzle assembly (Fig. 4) was traversed in discrete steps during the testing to vary the distance (L) between the primary jet nozzle exit plane and the radially positionable pitot pressure and gas sampling probe. An O-ring seal system isolates the flow in the duct from the atmosphere.

The nozzle assembly includes a circular, 0.524-in.-diam central nozzle, which introduces the high subsonic velocity, primary air jet, and an annular secondary injector assembly through which the outer hydrogen stream enters the duct. The duct-to-jet radius ratio (R_s/R_p) is 10. Details of the primary flow nozzle are shown in Fig. 5. In Fig. 4, it is seen that the secondary flow must pass through two porous plates and a screen. The two porous plates were installed to reduce the total pressure of the secondary stream to appropriate levels. The screen with 57-percent porosity was installed to distribute the secondary mass flow uniformly at the primary nozzle exit station.

3.2 INSTRUMENTATION

3.2.1 Pressure and Temperature Measurement

A pitot pressure and gas sampling probe having both upstream and downstream facing probe tips was installed in the duct at a fixed axial position. The probe can be traversed radially across the duct by a geared drive mechanism. The probe dimensions are shown in Fig. 6. By combining the motion of the axial-traversing nozzle assembly and the radially traversing probe, axial and radial surveys were made of the jet mixing and recirculating flow fields. In addition to the pitot probe assembly, a total of 50 static pressure orifices were installed along the duct wall, the majority of which were spaced about one inch apart, in a helical pattern that completes one revolution of the duct in a distance of 45.5 in. Orifices are spaced closer than one inch in the vicinity of the probes. Both static pressure and gas samples were obtained through the wall orifices. The static pressure orifices were connected to a water-filled manometer board which was photographed during the tests. When gas composition measurements were required at the wall, a scanner valve system connected the wall orifices to the gas concentration measurement system. Additional wall orifices were in the planes of the tips of the pitot probes, and measurements from these were utilized in the calculation of average axial velocity.

Probe pitot (total) pressures were measured using a system composed of two transducers. In the pressure differential range from 0 to 10 mm of mercury, the pitot pressures were sensed with a variable capacitance transducer, while in the range from 10 to 215 mm of mercury the pitot pressures were sensed by a 0- to 4-psi strain-gage transducer. Because of the sensitivity of the transducer used to measure the lower range of the pitot pressure, axial velocities lower than 100 ft/sec in pure hydrogen or velocities less than 25 ft/sec in pure air could not be accurately measured.

Temperatures were measured using copper-constantan thermocouples. The temperatures recorded during testing were the total temperature of the gaseous supplies of primary and secondary fluid, and they were measured upstream of critical-flow venturis, which were used to meter the primary and secondary mass flows. The venturis were calibrated so that their discharge coefficients were known over the ranges of metered mass flow encountered during the test program.

3.2.2 Gas Concentration Measurements

Concentrations of hydrogen in gas samples were measured using a system of gas-sample-driven, fluidic oscillators. The theory and use of fluidic oscillator systems to measure gas concentrations is described in Refs. 20, 21, and 22. The output frequency of a fluidic oscillator depends on the temperature and molecular weight of the gas sample passing through the oscillator, the specific construction of the oscillator, and the pressure drop across the oscillator. However, through calibration, the oscillator output frequency can be established as only a function of the molecular weight of the gas sample passing through the oscillator. Calibration of the fluidic oscillator system was accomplished using gas samples of air, hydrogen, and mixtures of nitrogen and hydrogen having molecular weights of 20 and 10.

3.3 TEST PROCEDURE

The pressure and concentration instrumentation was calibrated before each test by applying to each system a set of known pressures and concentrations and recording the corresponding instrumentation output values from each system. The sensitivity of each measurement system was obtained over ranges of values expected during testing.

The calibration data and the data taken during each test were recorded on seven-track, incremental, magnetic tape by a programmable

Hewlett-Packard 2010 data acquisition system (Ref. 23). In special instances, in order to obtain strictly qualitative information, probe pitot pressures and selected wall static pressures (sensed by 0 to 10 mm of mercury variable capacitance transducers) were displayed on an X-Y recorder.

At the beginning of a test, the desired primary and secondary mass flow rates were established by setting and monitoring appropriate air and hydrogen gas supply pressures and temperatures upstream of the critical-flow venturis. The piston-like nozzle assembly was positioned at a desired distance from the probe. Data were recorded as the probe assembly was traversed across the flow in a series of discrete steps. The nozzle assembly was then moved 1.38 in. toward the probe, which corresponds to the distance separating the forward and reverse facing pitot probes (Fig. 6), and another radial survey was conducted. Thus, forward and aft facing probes surveyed a radial path at the same axial location relative to the nozzle assembly. Gas concentrations were sampled with the forward facing probe, and pitot pressures were taken with both forward and aft facing probes. The complete pitot pressure and gas concentration profiles at a given axial station, relative to the nozzle, were constructed from the surveys of the forward and aft facing probe tips at this station.

At the initiation of the hydrogen-air mixing experiments, radial surveys of pitot pressure and gas concentration were made across the duct from wall to wall to ensure that buoyancy forces would have a negligible effect on the mixing processes. The initial surveys confirmed that the flow fields were symmetrical about the centerline, and, for the tests reported herein, radial surveys of the flow fields were limited to $-0.15 \leq r/R_s \leq 0.85$. This procedure minimize hydrogen consumption and test time.

3.4 DETERMINATION OF THE PRIMARY JET NOZZLE FLOW CHARACTERISTICS

Before experimentation was initiated, a pitot pressure survey of the jet issuing from the primary nozzle was made to establish the velocity field at the inlet of the combustor, hence, to ensure that the primary jet velocity profile was symmetrical. Typical velocity profiles obtained in orthogonal surveys are shown in Fig. 7 and compared with a fully developed turbulent pipe flow profile at an equivalent Reynolds number.

3.5 PRECISION OF MEASUREMENTS

The uncertainty of a measured parameter was determined from the bias limits and precision indices of the instrumentation by the procedures developed in Ref. 24. Given the bias limits and precision indices associated with the measurement necessary to define any parameter (ϕ) the total uncertainty in ϕ is defined as

$$U_\phi = \pm (B_\phi + t_{95} S_\phi) \quad (35)$$

where

$$B_\phi = \sqrt{\sum_{i=1}^N \left(\frac{\partial \phi}{\partial \xi_i} B_{\xi_i} \right)^2} \quad (36)$$

is the bias limit for ϕ , and

$$S_\phi = \sqrt{\sum_{i=1}^N \left(\frac{\partial \phi}{\partial \xi_i} S_{\xi_i} \right)^2} \quad (37)$$

is the precision index for ϕ , and where ξ_i are the measured parameters which define ϕ ; that is,

$$\phi = \phi(\xi_i), i = 1, \dots, N \quad (38)$$

N is the number of measured parameters that define ϕ . The parameter t_{95} is the "95 percentile point for the two-tailed students "t" distribution."

The bias limits and precision indices of instruments vary with variations in the values of measured quantities. Therefore, representative test conditions were selected upon which to base the precision indices and bias limits. Typical bias limits, precision indices, and uncertainties in the fundamental, measured parameters and the axial velocity and hydrogen gas concentrations, which are calculated from the fundamental, measured parameters, are presented in Table 3.

4.0 RESULTS AND DISCUSSION

4.1 INTRODUCTION

The range of test conditions established in the hydrogen-air experiments is presented in Table 4. The conditions are taken as defining three sets of flows of approximately the same velocity ratio ($\bar{u} = u_{S_0} / u_p$). For the three sets of experiments, the data defining the axial velocity, hydrogen concentration, and wall static pressure fields are presented in Appendix A. The data have been shown (Ref. 7) to possess both differences from, and similarities to, the constant density, recirculating flow mixing data of Becker, Hottel, and Williams, and Barchilon and Curtet. In the present study, experimental profiles of axial velocity, hydrogen mass fraction, wall static pressure, and the stagnation points on the wall are compared with corresponding theoretical calculations. The theoretical calculations were made by

using the theoretical approach summarized in Section 2.0, after applying both viscosity models; that is, calculations were made with and without potential core simulation.

4.2 COMPARISON OF EXPERIMENTAL AND THEORETICAL PROFILES OF AXIAL VELOCITY

The comparisons between experimental and theoretical radial profiles of axial velocity are shown in Fig. 8 for the three sets of experiments. In general, the shapes of the calculated velocity profiles are in agreement with experiment and show a jet-like nature, as would be expected. The largest differences between calculated and experimental velocity profiles occur near the centerline of the duct. The comparisons between calculated and experimental velocity profiles do not demonstrate superiority of one viscosity model over the other. At some axial stations, the predictions made by using the viscosity model without potential core appear to be in closer agreement with experiment than the calculations made with potential core simulation. Conversely, at other axial stations, the reverse trends are observed. This behavior is noted in all three sets of comparisons.

To obtain the calculations made using the viscosity model with the potential core simulation, a considerable sacrifice was incurred in the rigor of the solution procedure. To obtain convergent solutions, the complete source term in the vorticity transport equation (Eq. (12)) had to be set to zero, i.e.,

$$d_{\omega} = 0 \quad (39)$$

Moreover, the value of λ in the formulation of the corner vorticity (Eq. (25)) was reduced by approximately 3 percent from the value used to make the calculations with a viscosity model without potential core simulation. Thus, λ changed from $\lambda = 3.25$ to $\lambda = 3.15$ when the viscosity models were changed from no potential core simulation to potential core

simulation. It was also determined that the values of λ required to make the theoretical calculations could not be determined by inspection of the primary jet exhaust velocity profile as proposed in Section 2.0. Instead, values of λ were obtained by trial-and-error calculation and comparison with experiment. The theoretical velocity profiles shown in Fig. 8 are, therefore, correlations of experiment rather than predictions since the values of λ necessary to make the computations could not be established beforehand.

4.3 COMPARISON OF EXPERIMENTAL AND THEORETICAL RADIAL PROFILES OF HYDROGEN MASS FRACTION

Radial distributions of hydrogen mass fraction obtained experimentally are compared with theoretical calculations in Fig. 9. The corresponding experimental hydrogen mass fractions obtained at the wall have been added to this figure. The experimental and theoretical distributions are not in satisfactory agreement, quantitatively, but do exhibit similar trends. For example, both the experimental and theoretical profiles indicate that the hydrogen mass fraction tends to reach a maximum in the interior of the field, not at the wall.

Where a comparison of data from tests C and D exists (Fig. 9b), a consistent difference is indicated by experimental data. The difference in the experimental data was determined to be caused by a calibration error in pre- and posttest calibrations of the pitot-gas sampling system for test D. The calibration error was accounted for in a consistent manner in reducing data from test D, but despite the correction procedure, the difference between tests C and D persists.

The radial profiles of hydrogen mass fraction decay smoothly into flat, uniform profiles for all velocity ratios. The theoretical concentration profiles show greater rates of decay, diffusion, and spreading than experiment. The calculations made using the viscosity

model with potential core simulation appear to agree somewhat closer with experiment in the near field, but are in worse agreement with experiment in the far field, when compared with the calculations made without potential core simulation. For both viscosity models, the theoretical calculations shown in Fig. 9 were made with a numerical, effective Schmidt number (Table 1) of

$$N_{Sc\tilde{\zeta}} = \mu_E / \rho D_{CE} = 0.7 \quad (40)$$

However, numerical experimentation (Ref. 7) showed that the theoretical predictions are not sensitive to variations of up to 42 percent in the value of the turbulent Schmidt number, $N_{Sc\tilde{\zeta}}$.

4.4 COMPARISON OF EXPERIMENTAL AND THEORETICAL AXIAL DISTRIBUTIONS OF AXIAL VELOCITY ON THE CENTERLINE

Axial distributions of time-averaged axial velocity on the centerline of the combustor simulator are presented in Fig. 10 for each of the characteristic velocity ratios (\bar{u}). The experimental data exhibit an unusual feature, namely, the existence of regions in the velocity field where relatively little change occurs in the centerline axial velocity, for $\bar{u} = 0.036$ and 0.07 . This feature appears as "bumps" in experimental centerline axial velocity decay curves. The constant density data reported by Becker, Hottel, and Williams (Ref. 4) exhibit centerline axial velocity decay characteristics somewhat similar to those in Fig. 10 obtained in the variable-density mixing experiments. On the other hand, the theoretical predictions show smooth decay for both viscosity models for all velocity ratios. The reasons for this nature of the experimental velocity fields are not known although it was shown in Ref. 7 that the distributions of dynamic pressure along the axis of the duct also decay smoothly for all velocity ratios. One satisfactory feature of the theoretical solutions is that they appear to decay to values in close agreement with experiment at large axial distances from the primary nozzle exit plane, for example, at $x/R_p \geq 120$.

4.5 COMPARISON OF EXPERIMENTAL AND THEORETICAL AXIAL DISTRIBUTIONS OF HYDROGEN MASS FRACTION ON THE WALL AND ON THE CENTERLINE

Comparisons of theoretical and experimental axial distributions of hydrogen mass fraction on the wall and on the centerline are presented in Fig. 11. The experimental data from tests E and F show considerable scatter at the wall near the primary jet exit plane. The reason for this scatter is not known but experimental investigation (Ref. 7) eliminated the possibility of air leaks around the nozzle assembly. An interesting feature of the experimental data is that the concentration potential core extends further downstream than the velocity potential core. The concentration potential core is defined as the length from the exit plane of the primary jet nozzle to the point on the axis of the system where hydrogen concentrations are first sensed. The concentration potential core appeared to be about 20 primary jet radii in length (Fig. 11), whereas the velocity potential core appeared to be about 10 to 12 primary jet radii in length (Fig. 10).

The theoretical calculations of the wall and centerline hydrogen mass fraction are in poor agreement with the experimental data for both viscosity models in the near field. Again, as in the comparisons between experimental and theoretical interior flow field hydrogen distributions, the theoretical computations of wall concentration show much greater spreading and diffusion of hydrogen than is observed experimentally. Note, however, that the theoretical calculations of wall concentration made using the viscosity model without potential core show good agreement with the experimental data in the far field, where the radial concentration profiles have flattened out. However, the calculated wall concentrations from the viscosity model that simulated the potential core regions clearly shows evidence of nonconservation of hydrogen mass fraction. Therefore, further use of this viscosity model will require additional development of computational mesh networks as outlined in Section 2.4.3.

4.6 COMPARISON OF EXPERIMENTAL AND THEORETICAL AXIAL DISTRIBUTIONS OF STATIC PRESSURE ALONG THE WALL

The experimentally determined static pressure distributions are compared with theoretical calculations, made using both viscosity models, in Fig. 12. Also shown in this figure are the maximum static pressures, or recovery pressures, that correspond to one-dimensional flow theory, neglecting, however, wall shear stresses. The maximum wall static pressures were calculated based on the experimental pressure and momentum flux conditions for each characteristic \bar{u} .

The pressure distributions computed with the two viscosity models do not compare well with one another nor with the experimental data in the near field. The calculated minimum pressures in near field pressure distributions increase as \bar{u} decreases in the computations made using a viscosity model without potential core modeling. But, the calculated minimum pressures in the near field static pressure distributions increase with increasing \bar{u} in the computations made with the viscosity model that attempts to account for laminar flow regions. The reason for this behavior is unknown. In the far field, however, where the static pressure approaches its maximum value, both sets of computations are in reasonable agreement with experimental data.

4.7 COMPARISON OF EXPERIMENTAL AND THEORETICAL AXIAL LOCATIONS OF STAGNATION POINTS ON THE WALL

Experimental data defining the axial velocity fields were interpolated to determine points of zero velocity in the three sets of flow fields. The locations of the zero velocity points in the flow fields are shown in Fig. 13. Because the points of zero velocity are difficult to determine experimentally, these data are the least accurate of all the experimental data presented herein. However, by using the data in Fig. 13, stagnation points on the wall were defined and are shown as

functions of \bar{u} in Fig. 14. Also shown in Fig. 14 are theoretical predictions of the stagnation point locations made using both viscosity models. The predictions of the forward stagnation points are in poor agreement with the data, quantitatively, but show the same qualitative trends, namely, the stagnation point location moves downstream as \bar{u} increases. The predicted rear stagnation point locations are in fair agreement with the data; however, the inaccuracy of the experimental data defining the rear stagnation point locations is too large to confirm whether or not rear stagnation point varies with \bar{u} as predicted by the theory.

Investigations (Refs. 4, 5, and 8) of constant density mixing flows have shown that the location of the forward stagnation point varies with the parameter C_T as shown in Fig. 15. On the other hand, the data (Refs. 4, 5, and 8) have not demonstrated the variation of the rear stagnation point location with C_T conclusively (see Fig. 15). To be consistent with the published results of the constant-density experiments, a variable-density Craya-Curtet parameter (C_T^*) was defined, consistent with the definition provided by Becker, Hottel, and Williams, as

$$C_T^* = u_k^*/u_o^{**} \quad (41)$$

where

$$u_k^* = \frac{\rho_p u_p R_p^2}{\rho_k R_s^2} \left[1 + \frac{\rho_s}{\rho_p} \frac{u_{s_o}}{u_p} \left(\frac{R_s^2}{R_p^2} - 1 \right) \right] \quad (42)$$

and

$$u_o^{**} = \left\{ \frac{\rho_p u_p^2 R_p^2}{\rho_o^* R_s^2} \left[1 + \frac{\rho_s}{\rho_p} \frac{u_{s_o}^2}{u_p^2} \left(\frac{R_s^2}{R_p^2} - 1 \right) - \frac{1}{2} \frac{\rho_s}{\rho_p} \frac{u_{s_o}^2}{u_p^2} \frac{R_s^2}{R_p^2} \right] - \frac{1}{2} u_k^{*2} \right\}^{\frac{1}{2}} \quad (43)$$

In this formulation, ρ_k^* and ρ_o^* represent mass and momentum averaged densities based on inlet conditions. In particular,

$$\rho_k^* = \rho_p \frac{\left[1 + \frac{\rho_s^2}{\rho_p^2} \frac{u_{s_o}^2}{u_p^2} \frac{R_s^2}{R_p^2} \right]}{\left[1 + \frac{\rho_s}{\rho_p} \frac{u_{s_o}^2}{u_p^2} \frac{R_s^2}{R_p^2} \right]} \quad (44)$$

and

$$\rho_o^* = \rho_p \frac{\left[1 + \frac{\rho_s^2}{\rho_p^2} \frac{u_{s_o}^2}{u_p^2} \frac{R_s^2}{R_p^2} \right]}{\left[1 + \frac{\rho_s}{\rho_p} \frac{u_{s_o}^2}{u_p^2} \frac{R_s^2}{R_p^2} \right]} \quad (45)$$

However, it should be pointed out that alternate definitions for ρ_k^* and ρ_o^* have been proposed (Ref. 25). Nevertheless, by using the above definitions of ρ_k^* and ρ_o^* , values of C_T^* were determined and are listed for all of the present experimental conditions in Table 4. The variation of the forward and rear stagnation point locations with C_T^* are compared with the results from the constant density experiments in Fig. 15. The data show that there are considerable qualitative differences between the constant density and variable density correlations. It could be argued that proper definitions of ρ_k^* and ρ_o^* were not provided by Eqs. (43) and (44). However, a recent study (Ref. 25) which has attempted to correlate constant density and variable density combustor flows using the C_T^* parameter but with different definitions for ρ_k^* and ρ_o^* had inconclusive results. Therefore, at present, suitable definitions for ρ_k^* and ρ_o^* to correlate constant-density and variable-density combustor flows do not exist. Hence, additional understanding appears necessary in order to formulate a useful variable-density confined mixing similitude parameter such as C_T^* .

5.0 CONCLUSIONS

An analysis of the literature revealed that before confident design of combustor processes based on recirculating flows can be provided, much more experimental and theoretical study of ducted, axisymmetric, turbulent jet mixing with recirculation is required. Detailed recommendations for future study and research of such flows are presented in Ref. 7. The present investigation obtained a set of detailed experimental data defining ducted, coaxial, variable-density turbulent jet mixing with recirculation. The primary or central jet was air, and the annular, secondary stream was hydrogen. The study provided the axial velocity, hydrogen concentration, and wall static pressure fields for three sets of recirculating flows for the hydrogen-to-air velocity ratios (0.02, 0.036, and 0.07). For these experiments, the density ratio of the hydrogen to the air was 0.069, and the mixing duct to jet radius ratio was 10.

The conclusions from the present investigation are:

1. The velocity fields obtained are, in general, similar to constant-density recirculating flow experiments with the exception that, at the velocity ratios of 0.036 and 0.07, "bumps" appeared in the centerline axial velocity decay curves.
2. The locations of the points of zero velocity in the flow field are difficult to measure, and for this reason, the characteristic flow stagnation point locations on the wall could only be tentatively defined. In the main, however, axial velocity, hydrogen concentration, and wall static pressure fields are sufficiently well defined that the data can serve for design of recirculating flow combustors or for the evaluation and development of predictive techniques for such flows.
3. The theoretical study of the variable-density, recirculating combustor flows showed that care must be taken and considerable effort expended to obtain reasonable calculations of such flows. Problems that remain to be overcome include the computation of the static pressure fields, construction of nonuniform mesh configurations within which routine calculations can be made with conservation of species assured, specification of vorticity at a protruding corner from which flow separates, such as at a nozzle lip, and, finally, the development of more accurate models for effective, turbulent or eddy, viscosity for variable-density flows. In general, the numerical solution procedure studied herein could not be considered a satisfactory predictive technique for engineering design calculations associated with such flows.

4. A variable-density correlation parameter (C_T^*), analogous to the Craya-Curtet parameter, was defined. The wall stagnation point locations were correlated with C_T^* for the three \bar{u} cases investigated. The correlation appeared quantitatively different than that for constant-density flows, and hence the utility of such a parameter for correlation of ducted, recirculating flows could not be determined.

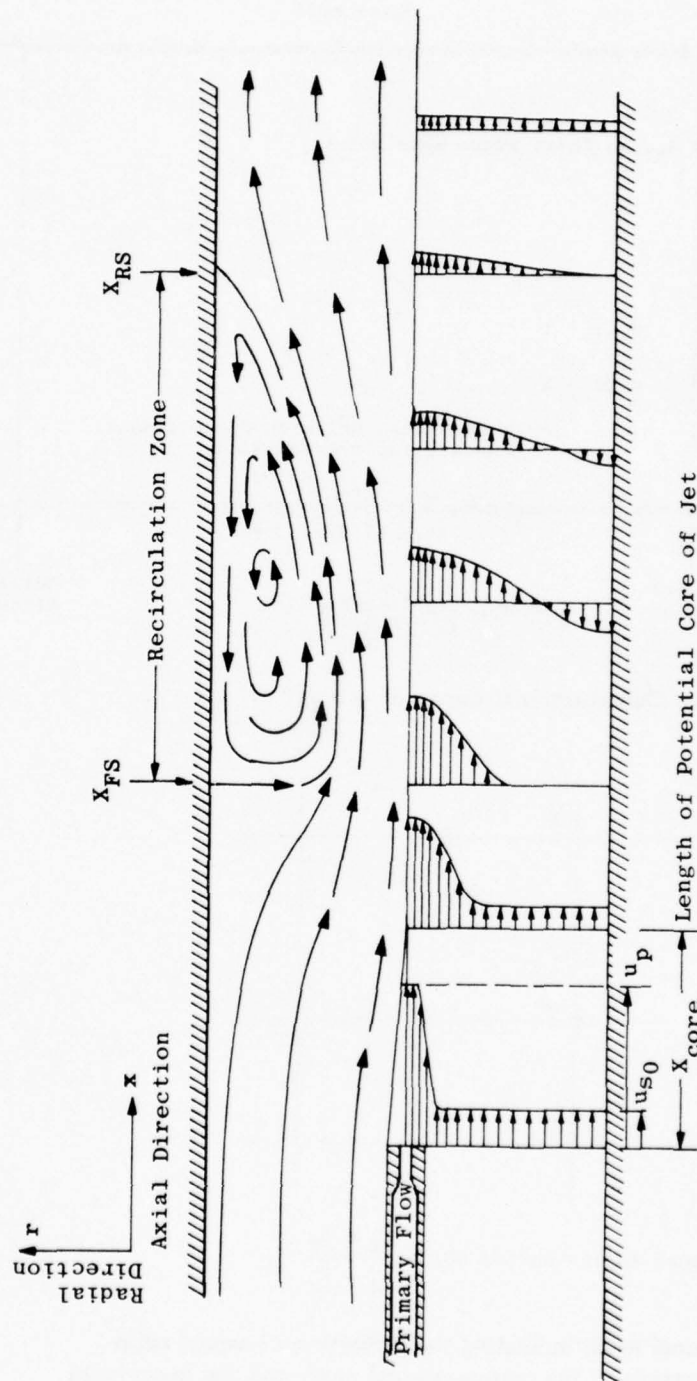
REFERENCES

1. Gosman, A. D., Pun, W. M., Runchal, A. K., Spalding, B. D., and Wolfshtein, M. Heat and Mass Transfer in Recirculating Flows. Academic Press, New York, 1969.
2. Thring, M. W. and Newby, M. P. "Combustion Length of Enclosed Turbulent Jet Flames." Proceedings of the Fourth Symposium (International) on Combustion, Williams and Wilkins, Vol. I, London, 1953.
3. Curtet, R. "Confined Jets and Recirculation Phenomena with Cold Air." Combustion and Flame, Vol. 2, No. 2, October-December 1958, pp. 383-411.
4. Becker, H. A., Hottel, H. C., and Williams, G. C. "Mixing and Flow in Ducted Turbulent Jets." Proceedings of the Ninth Symposium (International) on Combustion, Academic Press, Inc., Vol. I, New York, 1963, pp. 7-20
5. Becker, H. A., Hottel, H. C., and Williams, G. C. "Concentration Intermittency in Jets." Proceedings of the Tenth Symposium (International) on Combustion. The Combustion Institute, Pittsburg, 1965, pp. 1253-1263.

6. Becker, H. A., Hottel, H. C., and Williams, G. C. "Concentration Fluctuations in Ducted Turbulent Jets." Proceedings of the Eleventh Symposium (International) on Combustion. The Combustion Institute, Pittsburg, 1967, pp. 791-798.
7. Schulz, R. J. "An Experimental and Theoretical Investigation of Confined, Two-stream Variable Density, Turbulent Jet Mixing with Recirculation." Ph.D. dissertation, The University of Tennessee, Knoxville, 1976.
8. Barchilon, M. and Curtet, R. "Some Details of the Structure of an Axisymmetric Confined Jet with Backflow." Transactions of the ASME Journal of Basic Engineering, Vol. 86, December 1964, pp. 777-787.
9. Roache, P. J. Computational Fluid Dynamics. Hermosa Publishers, Inc., Albuquerque, New Mexico, 1972.
10. Scaccia, C., and Kennedy, L. A. "Mixing of Coaxial Jets in a Confined Tube." Developments in Mechanics; Proceedings of the Thirteenth Midwestern Mechanics Conference, J. L. Abrams, et al., editors, Vol. 7, The University of Pittsburgh School of Engineering, Pittsburgh, 1973, pp. 95-109.
11. Schlichting, H. Boundary Layer Theory. Sixth Edition, McGraw-Hill Book Company, Inc., New York, 1966.
12. Harsha, P. T. "Free Turbulent Mixing: A Critical Evaluation of Theory and Experiment." Ph.D. dissertation, The University of Tennessee, Knoxville, 1970.
13. Launder, B. E. and Spalding, D. B. Mathematical Models of Turbulence. Academic Pressure, Inc., New York, 1972.

14. Harlow, F. H. (ed.). Turbulence Transport Modeling: AIAA Selected Reprints Series. The American Institute of Aeronautics and Astronautics, Vol. 14, New York, 1973.
15. Patankar, S. V. and Spalding, B. D. Heat and Mass Transfer in Boundary Layers. Second Edition, International Textbook Company, Ltd., London, 1970.
16. Kline, S. J., Morkovin, M. V., Sovran, G., and Cockrell, D. J. (eds.). Proceedings of the 1968 AFOSR-IFP Stanford Conference on Computation of Turbulent Boundary Layers. Vol. I, The Thermosciences Division of the Department of Mechanical Engineering, Stanford University, Palo Alto, California, 1968.
17. Rodi, W. "The Prediction of Free Turbulent Boundary Layers by the Use of a Two-Equation Model of Turbulence." Ph.D. dissertation, The University of London, London, England, 1972.
18. Birch, S. F., Rhudy, D. H., and Bushness, D. M. (eds.). Proceedings of the 1972 Langley Conference on the Computation of Free Turbulent Shear Layers. Vol. 1, NASA SP-301, 1972.
19. Hill, P. G. "Turbulent Jets in Ducted Streams." Journal of Fluid Mechanics, Part I, Vol. 22, May 1964, pp. 161-186.
20. Rhodes, R. P. "Probing Techniques for Use in High Temperature Reacting Flows." AEDC-TR-68-44 (AD829143), March 1968.
21. LeRoy, M. J., Jr., and Gorland, S. H. "Sensing Molecular Weights of Gases with a Fluidic Oscillator." NASA TMX-1939, 1974.

22. Riddlebaugh, S. M. "Use of the Fludic Oscillator to Measure Fuel-Air Ratios of Combustion Gases." NASA TM X-3068, 1974.
23. Hewlett-Packard Data Acquisition System, Models 3010 K,L. First Edition, Hewlett-Packard Company, Palo Alto, California, 1968.
24. Abernethy, R. B., et al., Pratt and Whitney Aircraft, and Thompson J. W., Jr., ARO, Inc. "Handbook-Uncertainty in Gas Turbine Measurements." AEDC-TR-73-5 (AD755356), February 1973.
25. Guruz, A. G., Guruz, H. K., Osuwan, S., and Steward, F. R. "Aerodynamics of a Confined Burning Jet." Combustion Science and Technology, Vol. 9, No. 3 and 4, 1974, pp. 103-110.



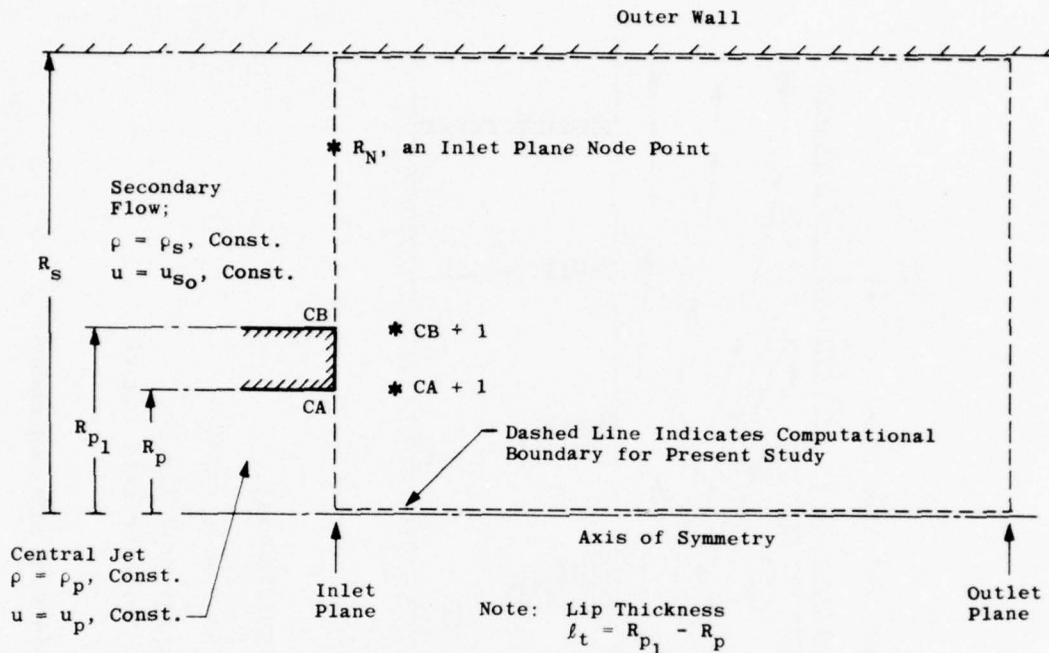
u_p is the primary jet velocity at nozzle exit.

u_{s0} is the secondary jet velocity at nozzle exit.

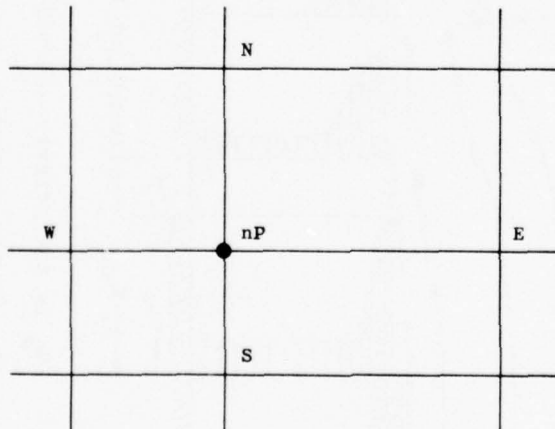
Mean streamline pattern shown in upper half figure.

Mean axial velocity profiles shown in lower half figure.

Figure 1. Schematic of turbulent ducted mixing with recirculation.



a. Computational region of interest



$$\text{Local Aspect Ratio, } AR, = \frac{x_E - x_W}{r_N - r_S}$$

b. Computational mesh indicating the definition of aspect ratio

Figure 2. Configuration of the computational mesh and the boundaries of the region encompassing the recirculating flows.

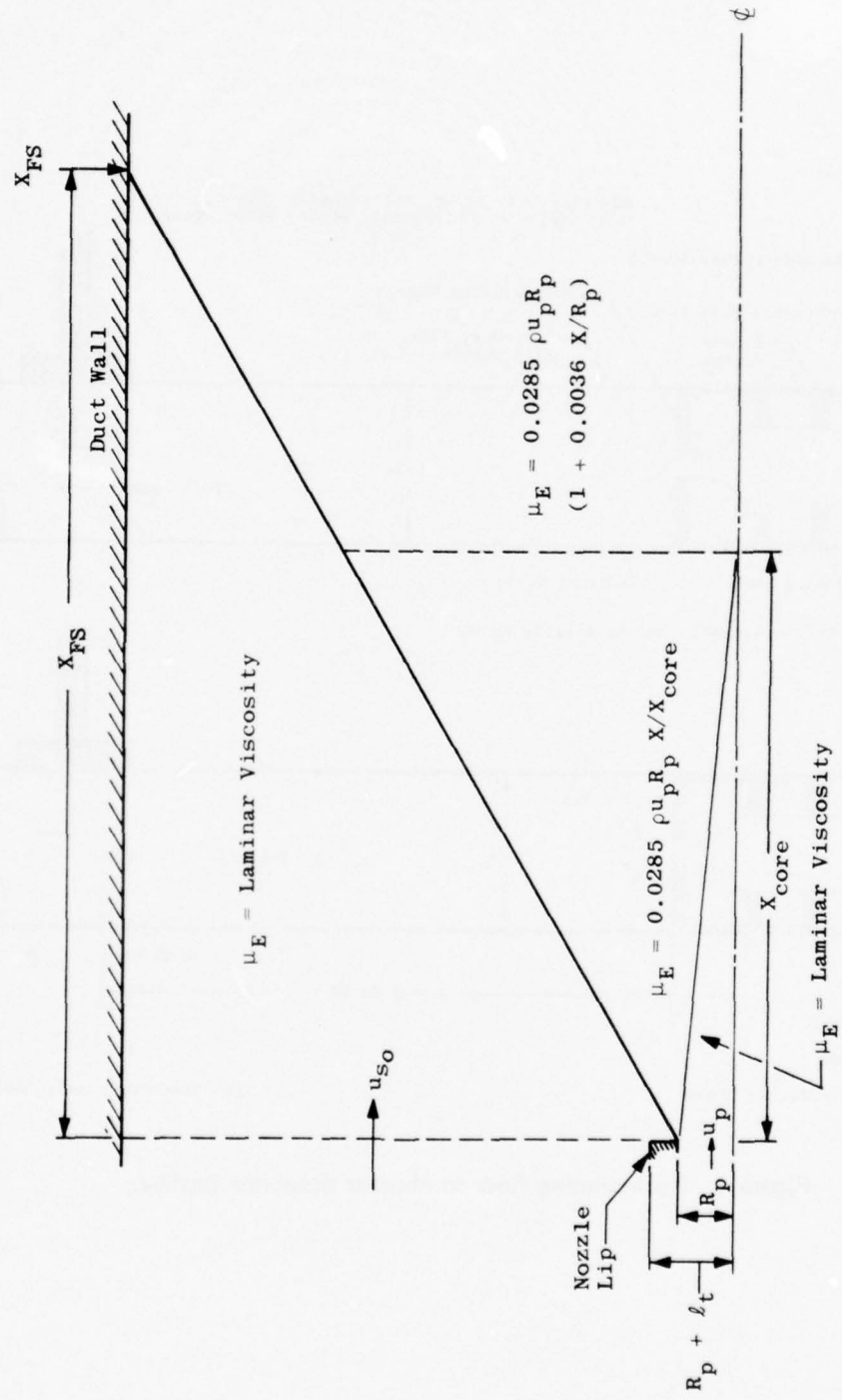


Figure 3. Eddy viscosity distribution for confined recirculating flows which includes potential flow regions.

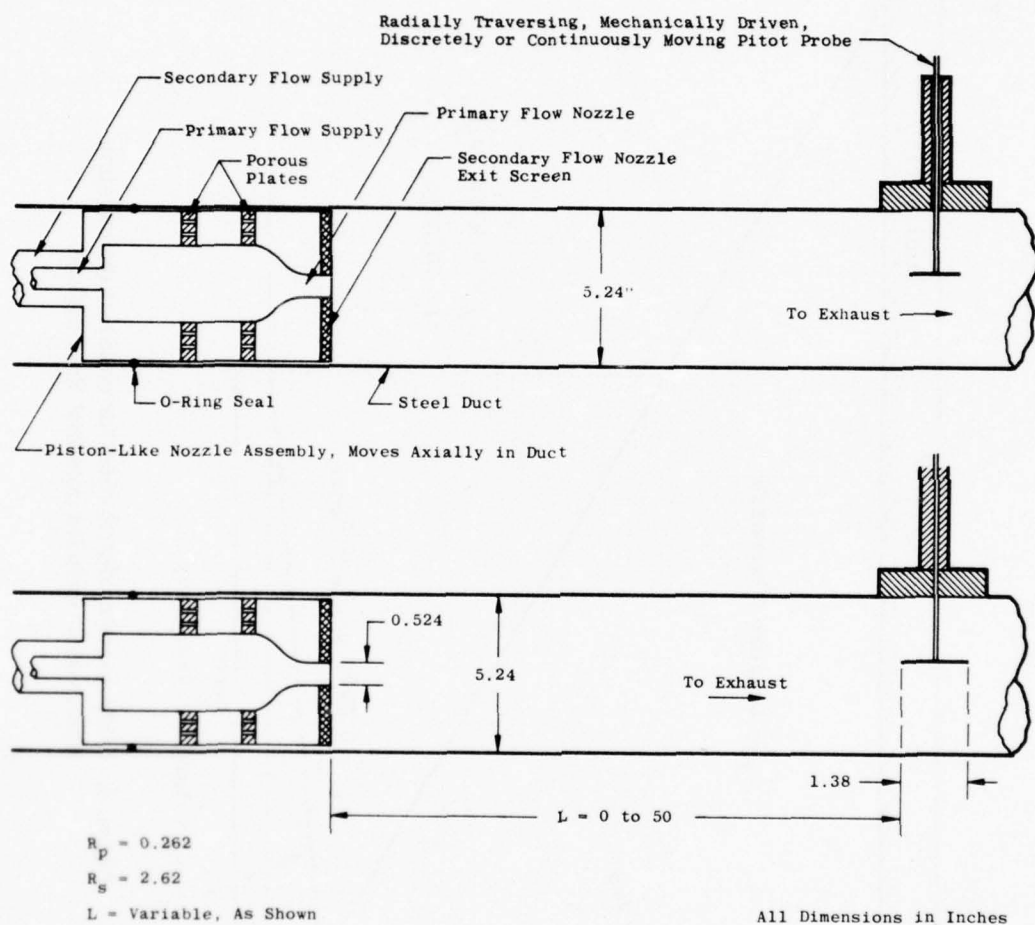


Figure 4. Recirculating flow combustor simulator facility.

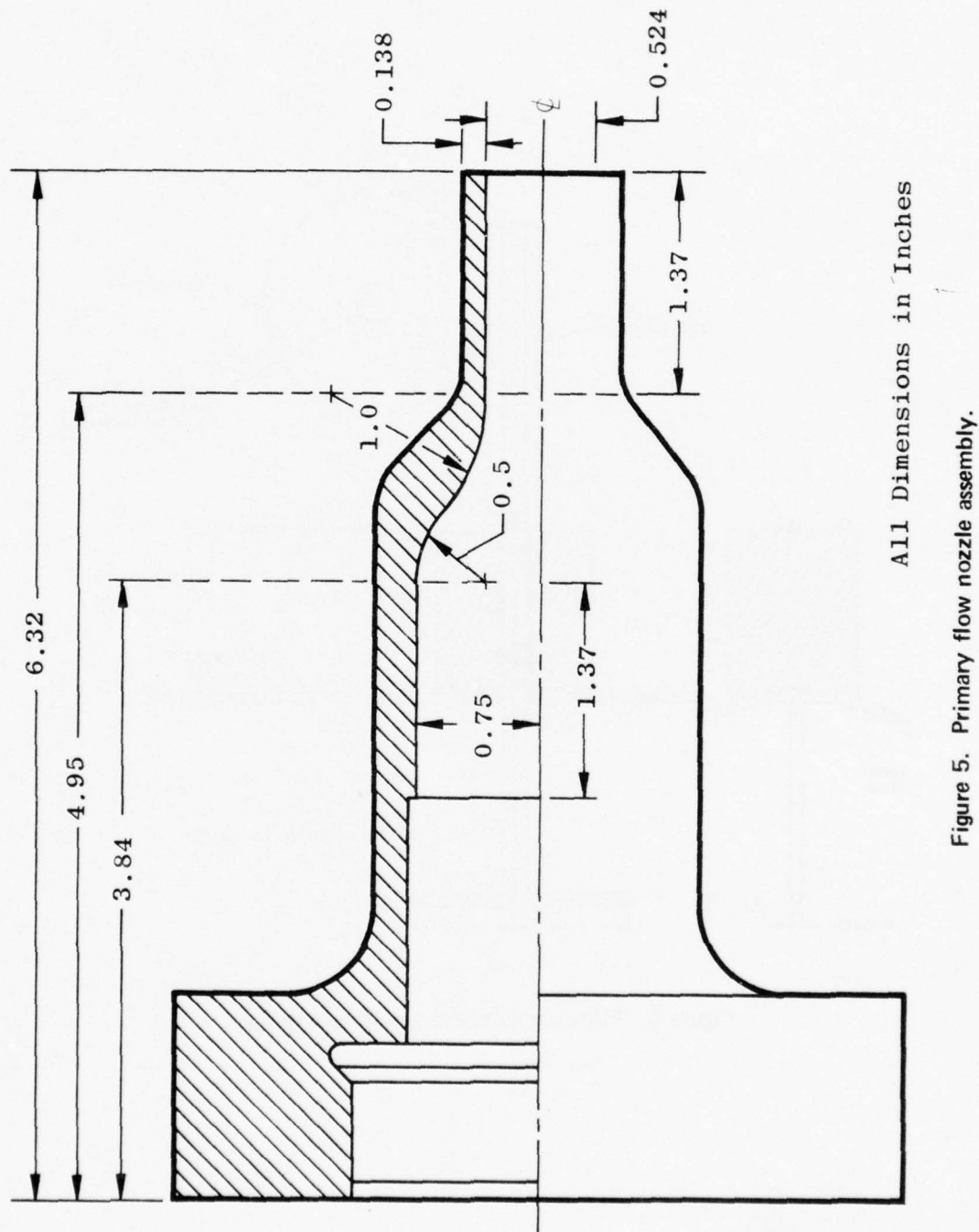


Figure 5. Primary flow nozzle assembly.

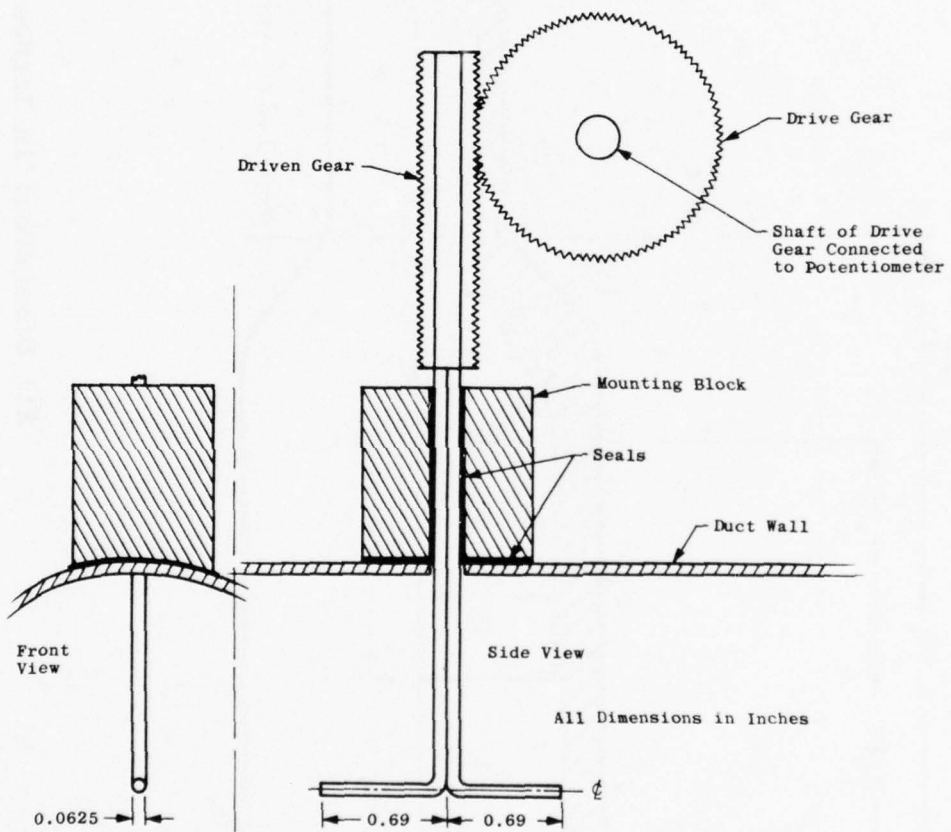


Figure 6. Pitot pressure and gas sample probe.

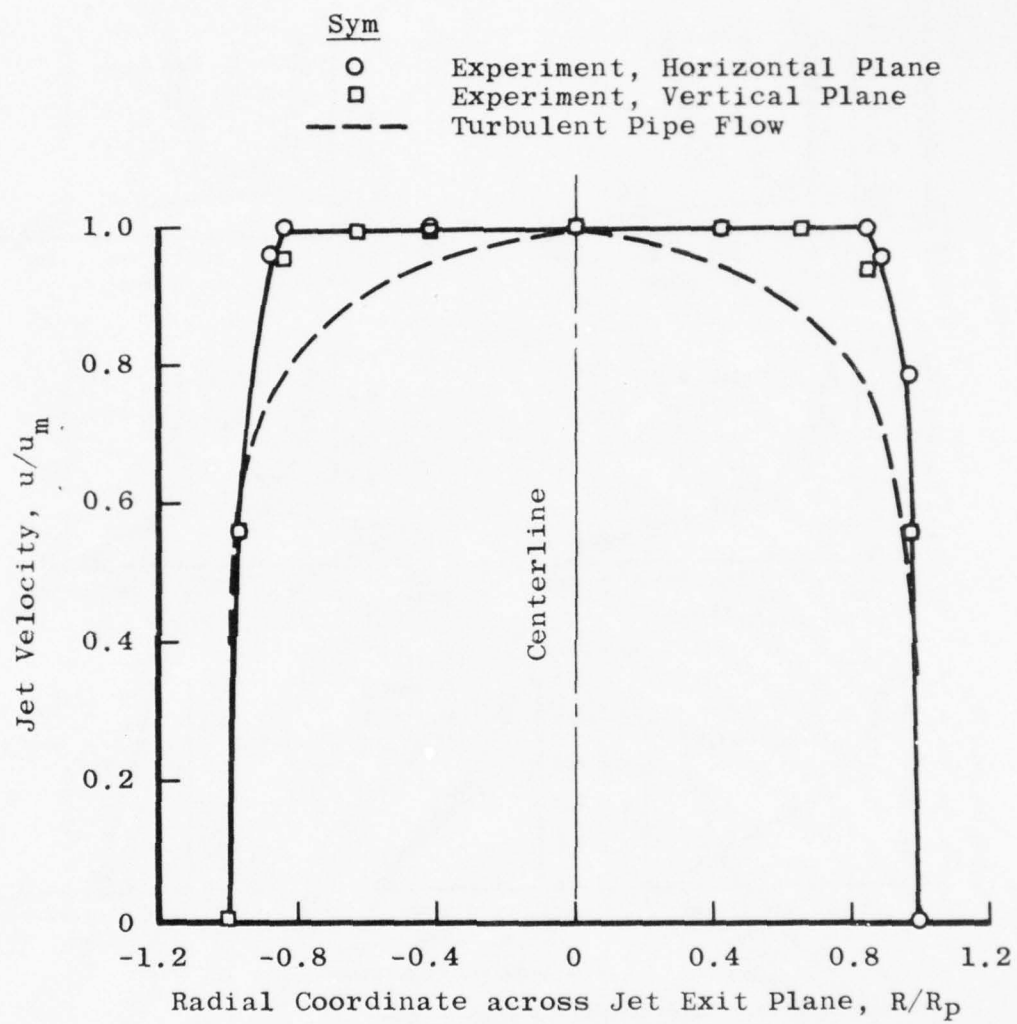
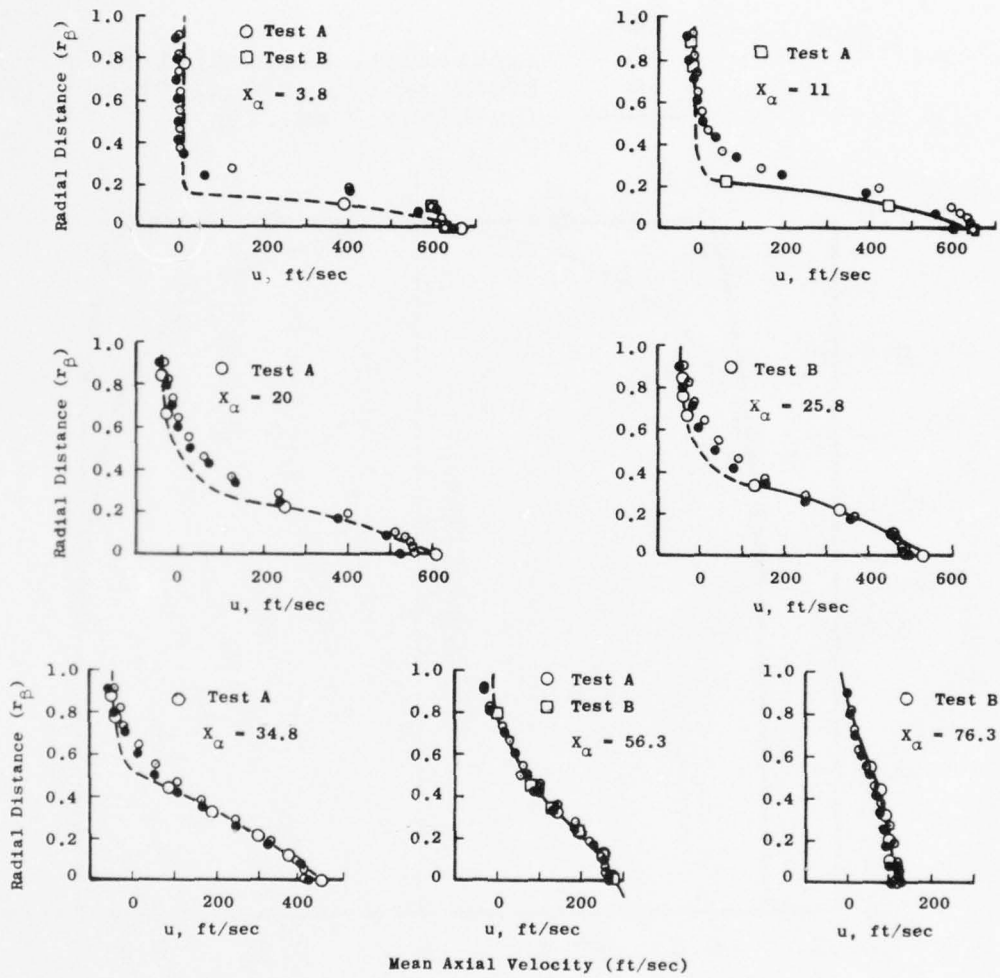


Figure 7. Primary jet exit velocity profiles compared with turbulent pipe flow profile at the same Reynolds number, $N_{ReD} = 10^5$.

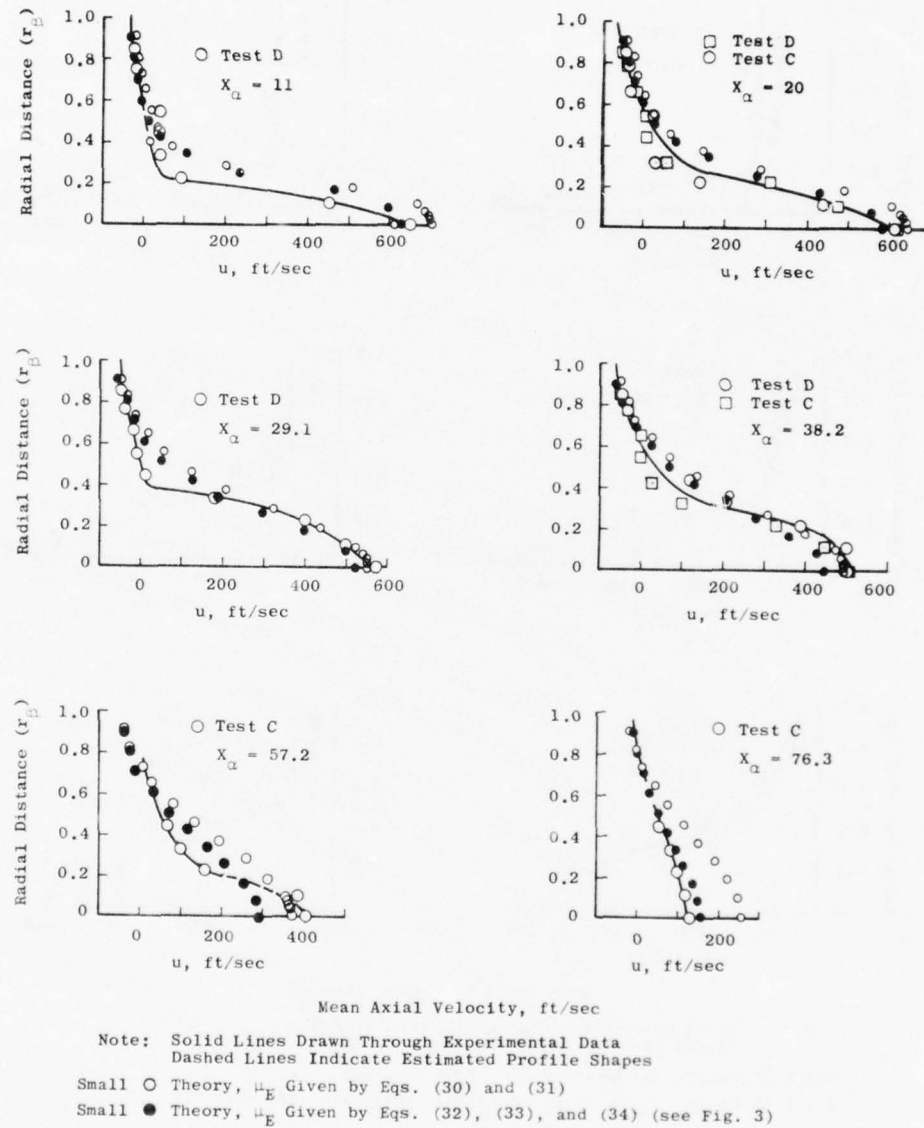


Note: Solid Lines Drawn Through Experimental Data
Dashed Lines Indicate Estimated Profile Shapes

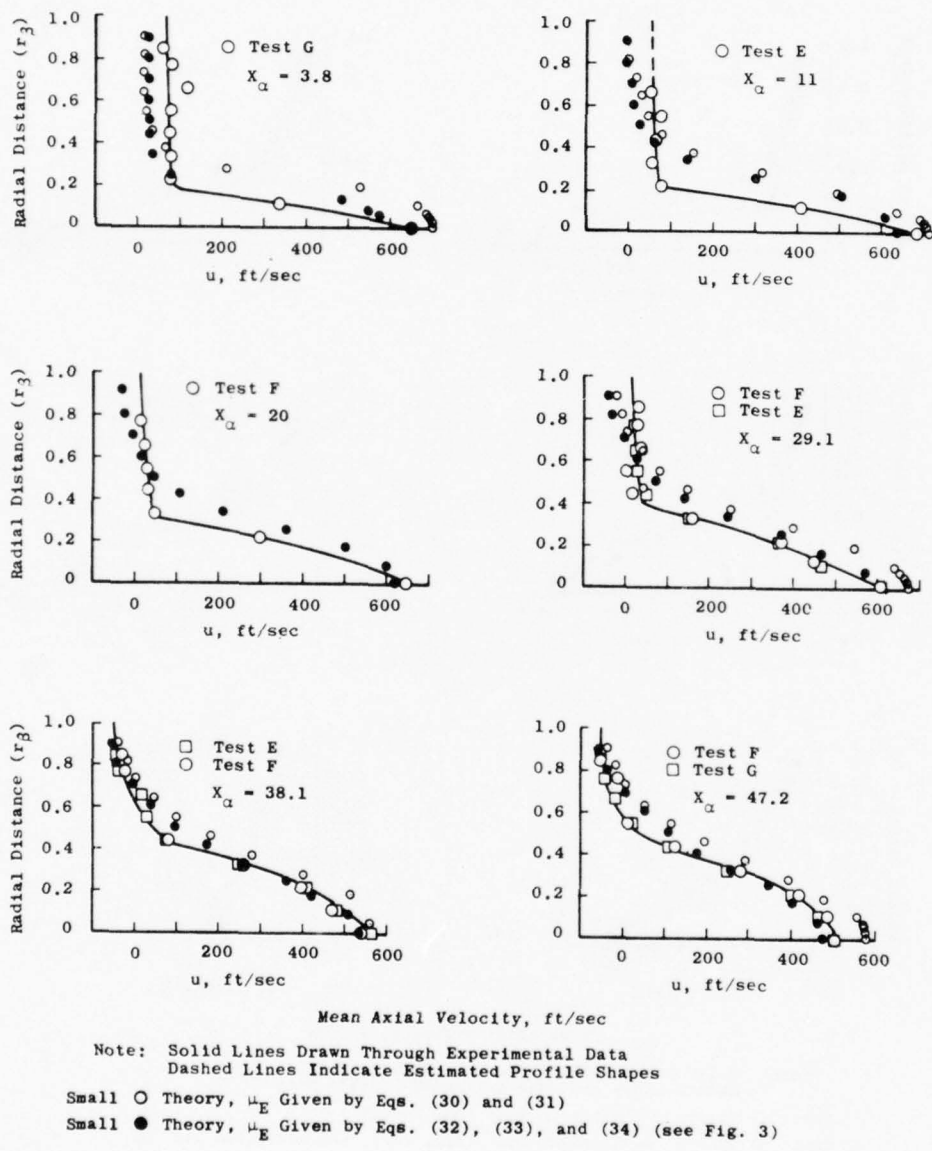
Small \circ Theory, μ_E Given by Eqs. (30) and (31)
Small \bullet Theory, μ_E Given by Eqs. (32), (33), and (34) (see Fig. 3)

a. $\bar{u} = 0.02$

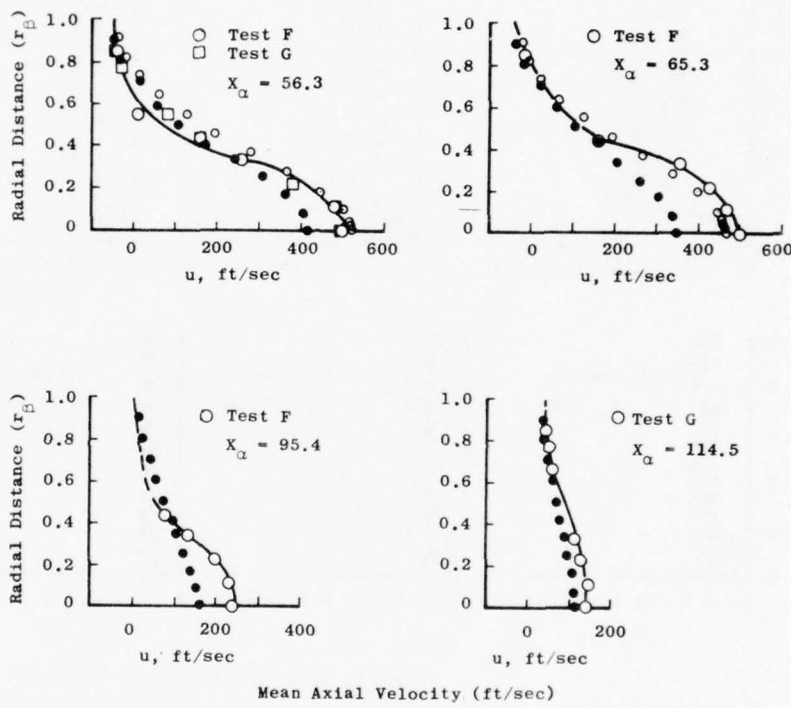
Figure 8. Comparison of experimental and theoretical radial distributions of mean axial velocity.



b. $\bar{u} = 0.036$
Figure 8. Continued.



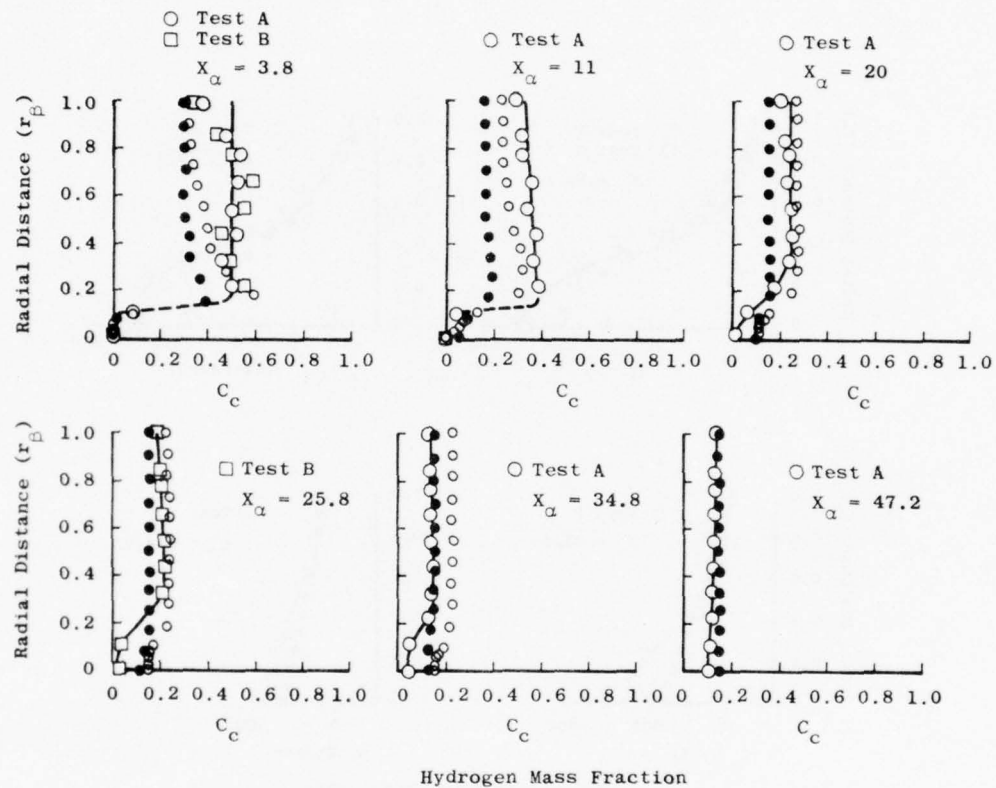
c. Concluded
Figure 8. Continued.



Note: Solid Lines Drawn Through Experimental Data
Dashed Lines Indicate Estimated Profile Shapes

Small ○ Theory, μ_E Given by Eqs. (30) and (31)
Small ● Theory, μ_E Given by Eqs. (32), (33), and (34) (see Fig. 3)

c. $\bar{u} = 0.07$
Figure 8. Concluded.



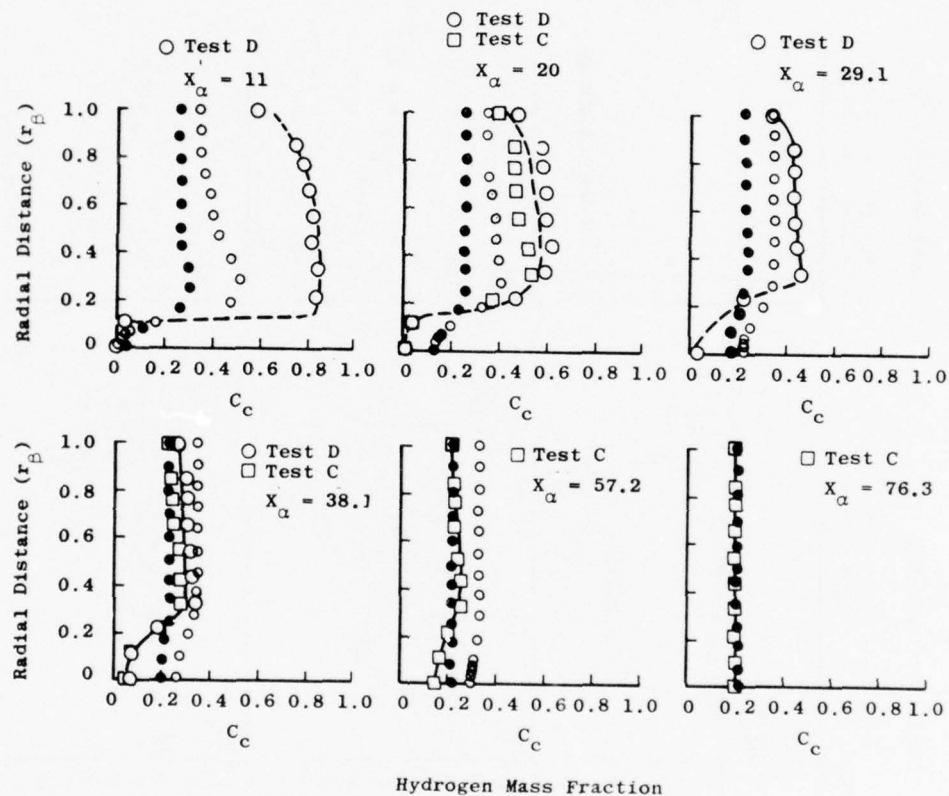
Note: Solid Lines Drawn Through Experimental Data
Dashed Lines Indicate Estimated Profile Shapes

Small \circ Theory, μ_E Given by Eqs. (30) and (31)

Small \bullet Theory, μ_E Given by Eqs. (32), (33), and (34) (see Fig. 3)

a. $\bar{u} = 0.02$

Figure 9. Comparison of experimental and theoretical radial distributions of mean hydrogen mass fraction.



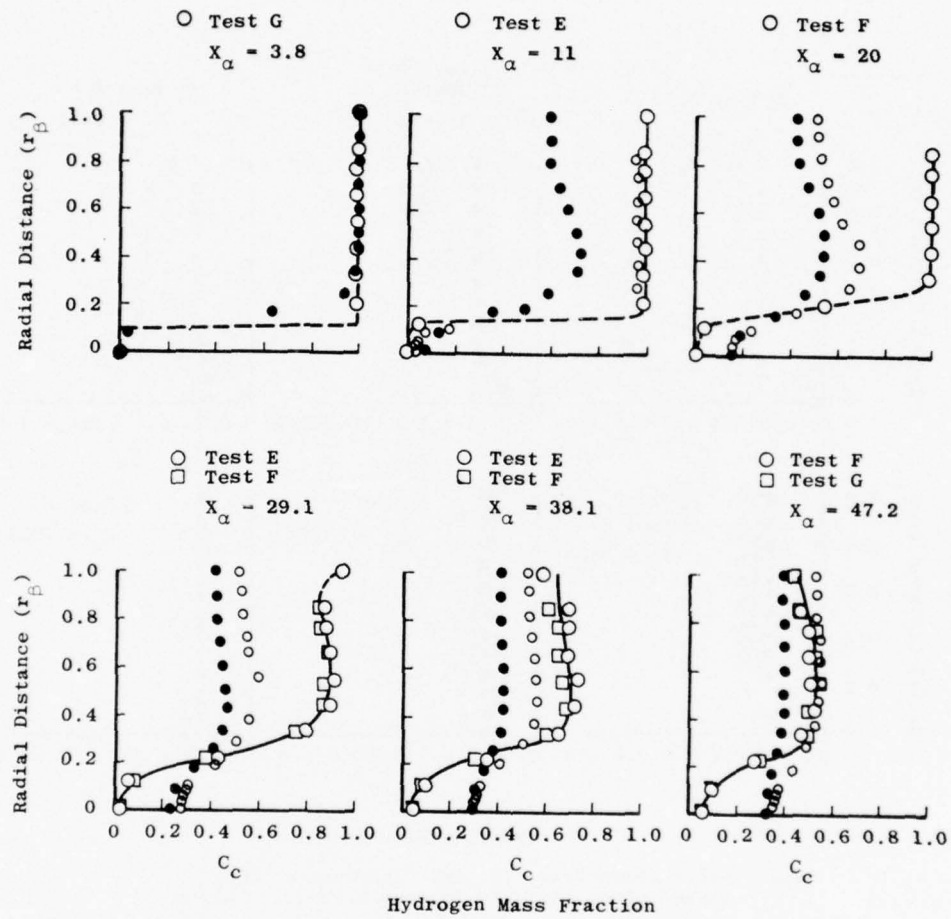
Note: Solid Lines Drawn Through Experimental Data
Dashed Lines Indicate Estimated Profile Shapes

Small ○ Theory, μ_E Given by Eqs. (30) and (31)

Small ● Theory, μ_E Given by Eqs. (32), (33), and (34) (see Fig. 3)

b. $\bar{u} = 0.036$

Figure 9. Continued.

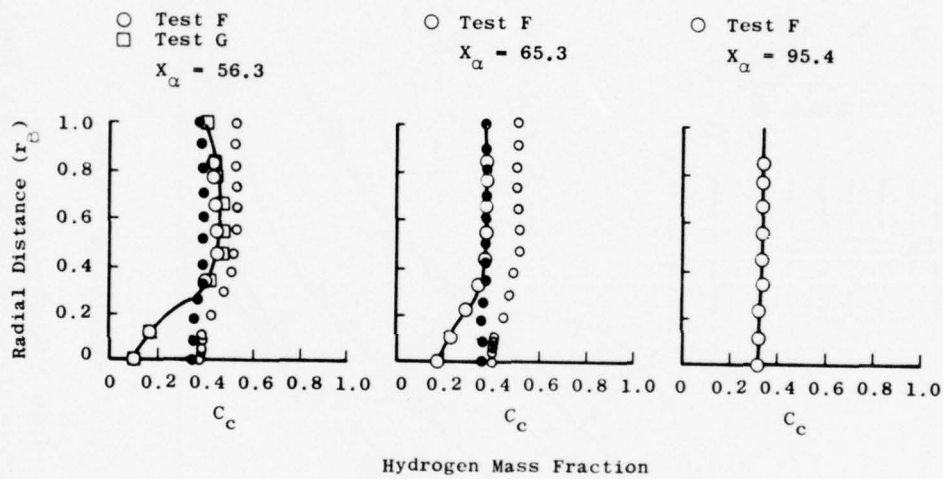


Note: Solid Lines Drawn Through Experimental Data
Dashed Lines Indicate Estimated Profile Shapes

Small \circ Theory, μ_E Given by Eqs. (30) and (31)
Small \bullet Theory, μ_E Given by Eqs. (32), (33), and (34) (see Fig. 3)

$$c. \bar{u} = 0.07$$

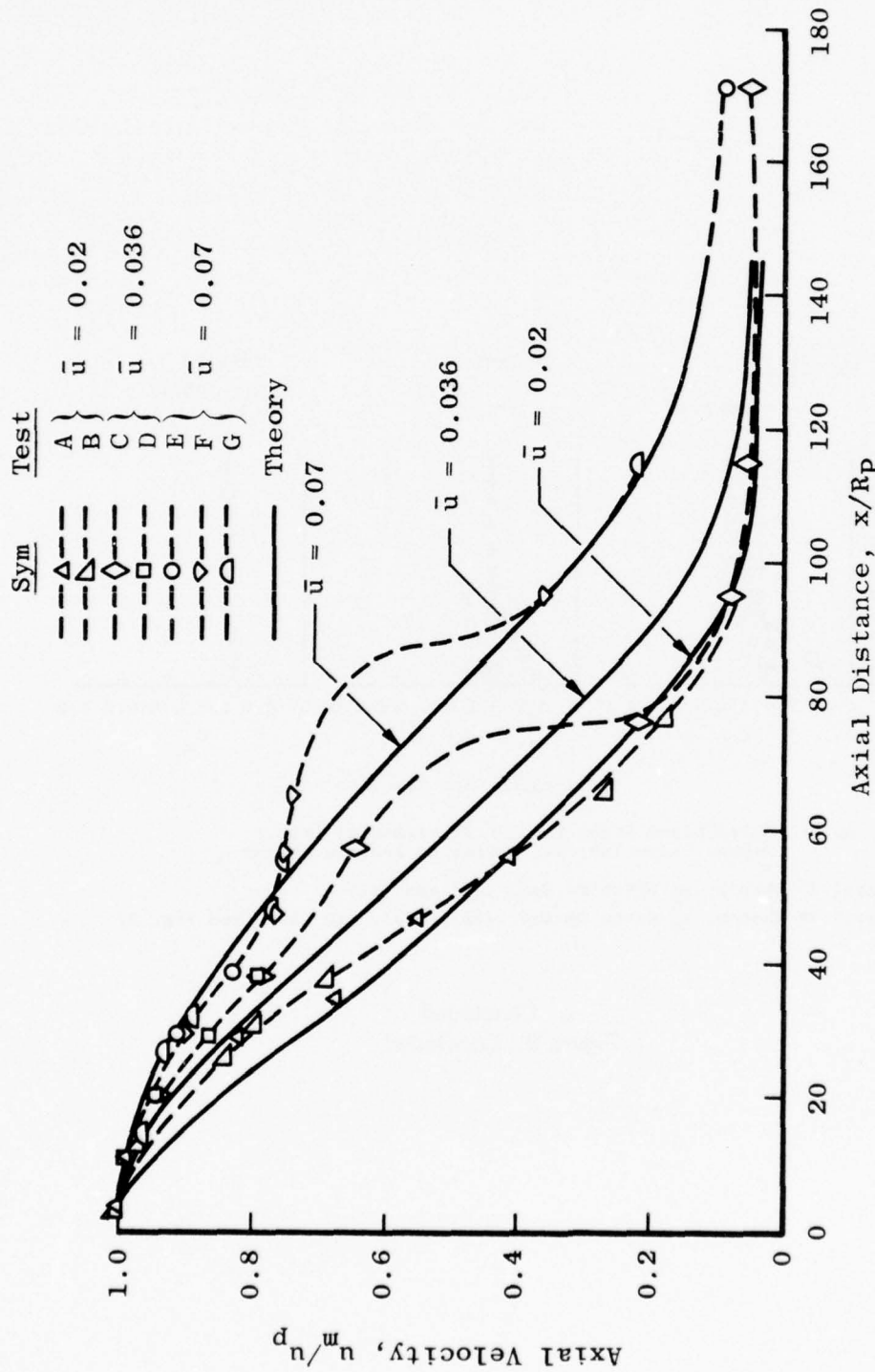
Figure 9. Continued.



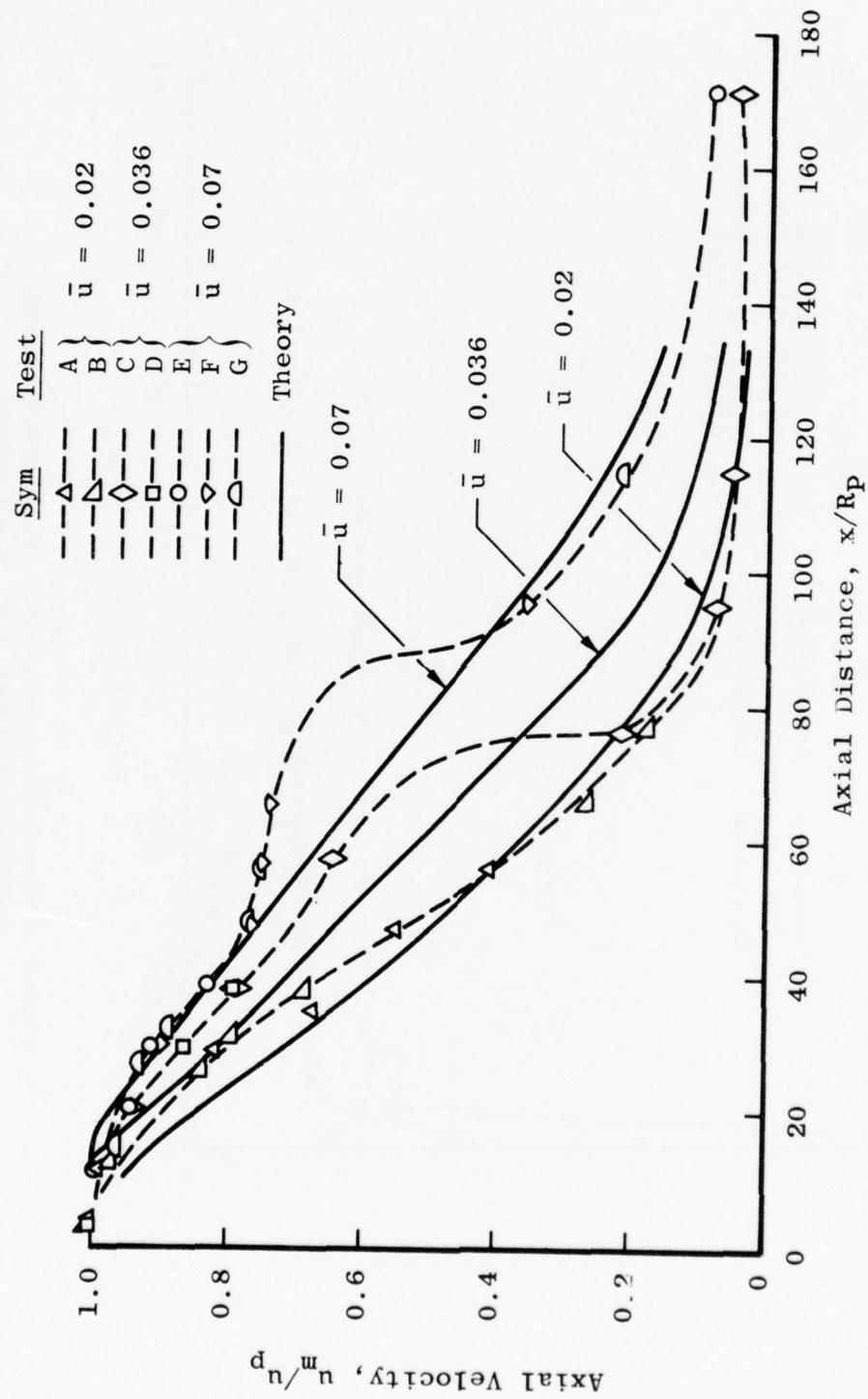
Note: Solid Lines Drawn Through Experimental Data
Dashed Lines Indicate Estimated Profile Shapes

Small \circ Theory, μ_E Given by Eqs. (30) and (31)
Small \bullet Theory, μ_E Given by Eqs. (32), (33), and (34) (see Fig. 3)

c. Concluded
Figure 9. Concluded.



a. Viscosity model without potential core
 Figure 10. Comparison of experimental and theoretical axial distributions
 of nondimensionalized mean axial velocity on the centerline of
 the combustor simulator.



b. Viscosity model with potential core
 Figure 10. Concluded.

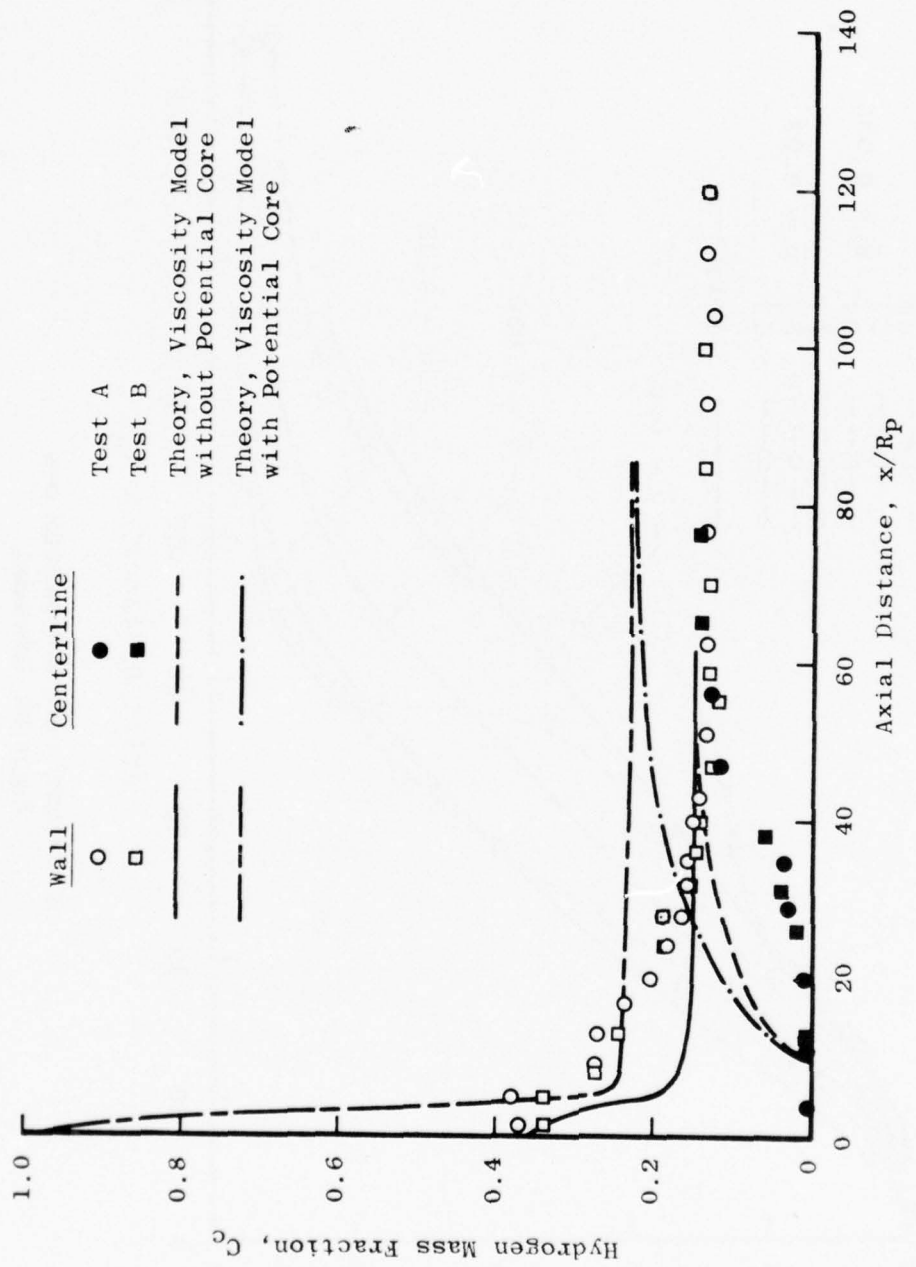


Figure 11. Comparison of experimental and theoretical axial distributions of hydrogen mass fraction at the wall and centerline.
a. $\bar{u} = 0.02$

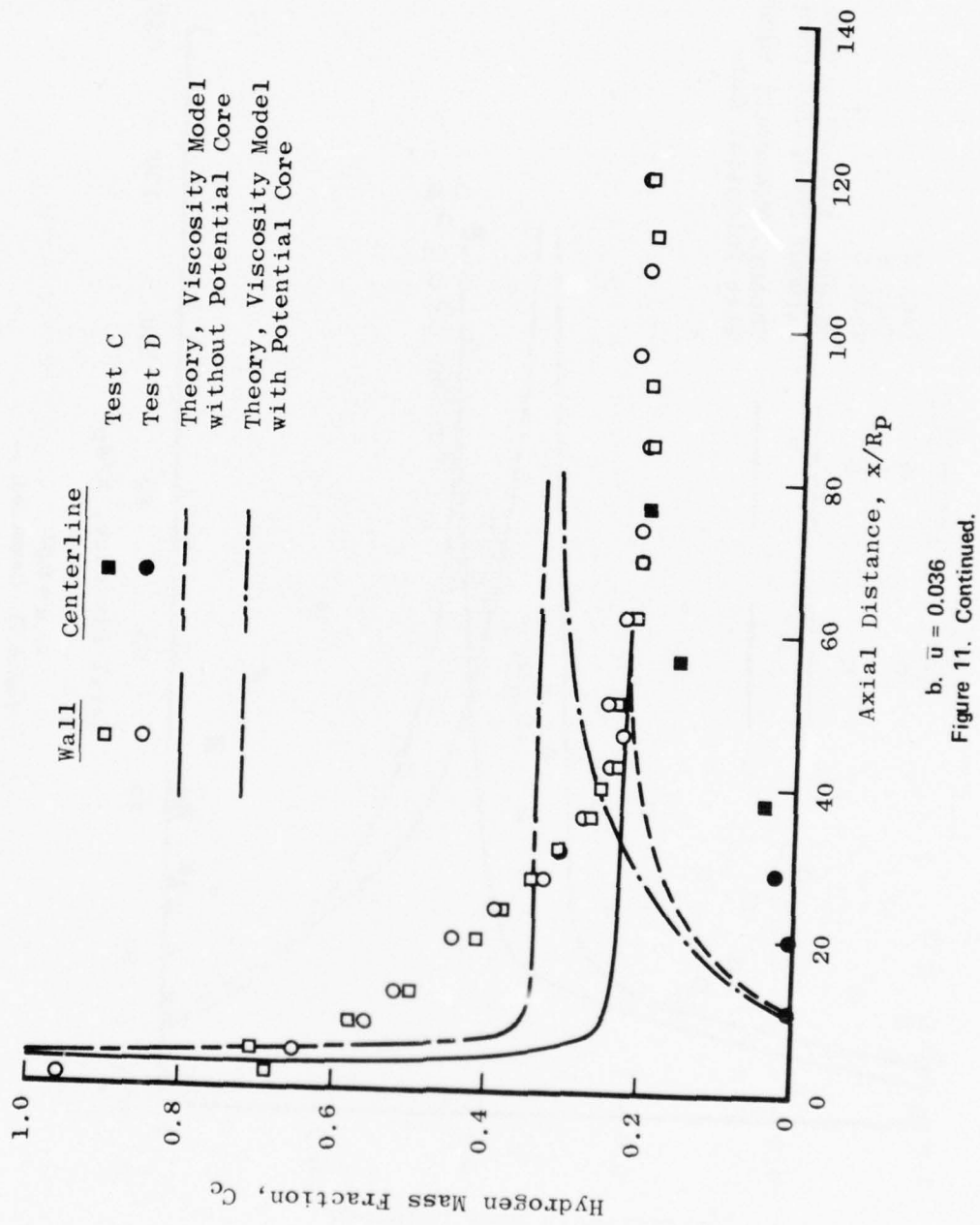
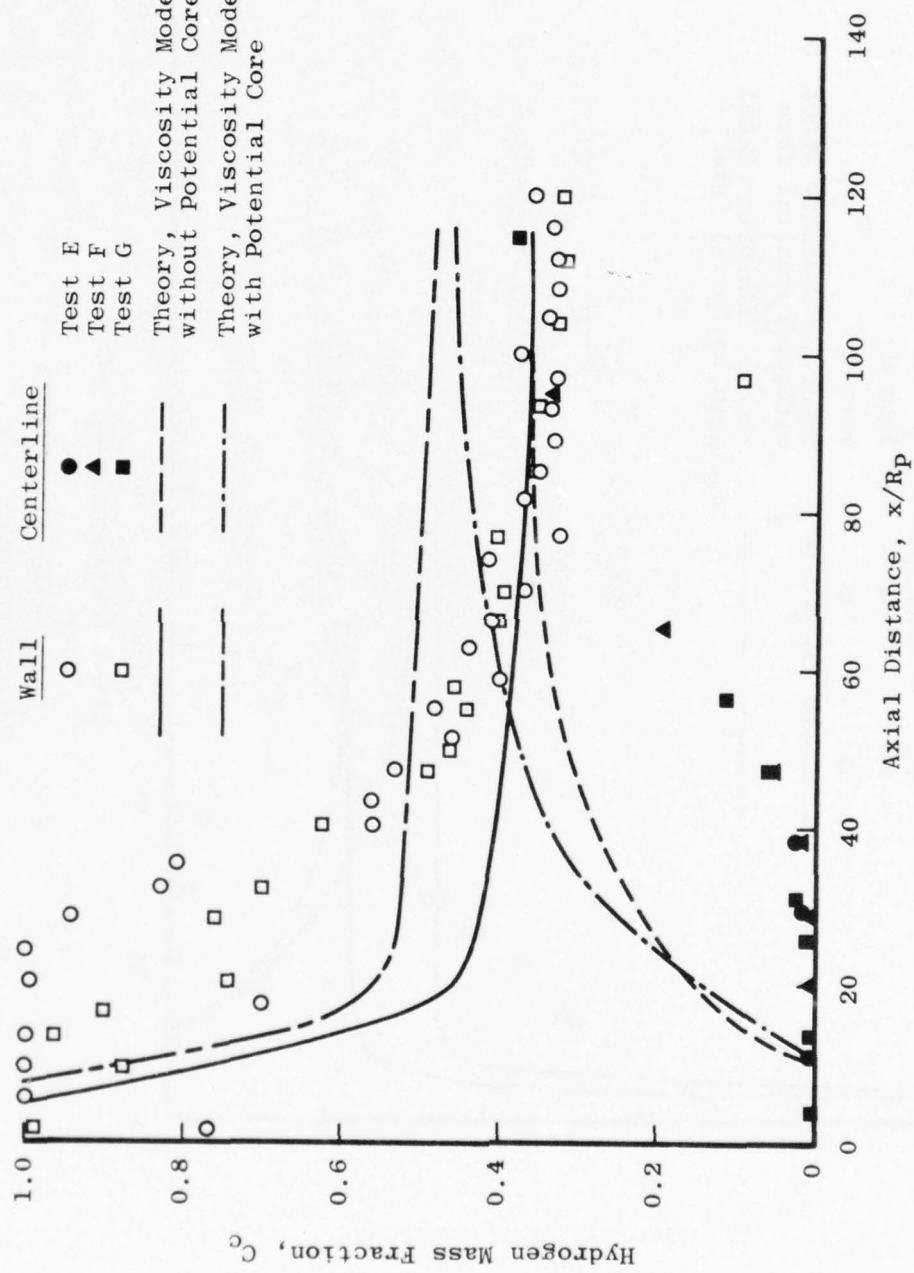
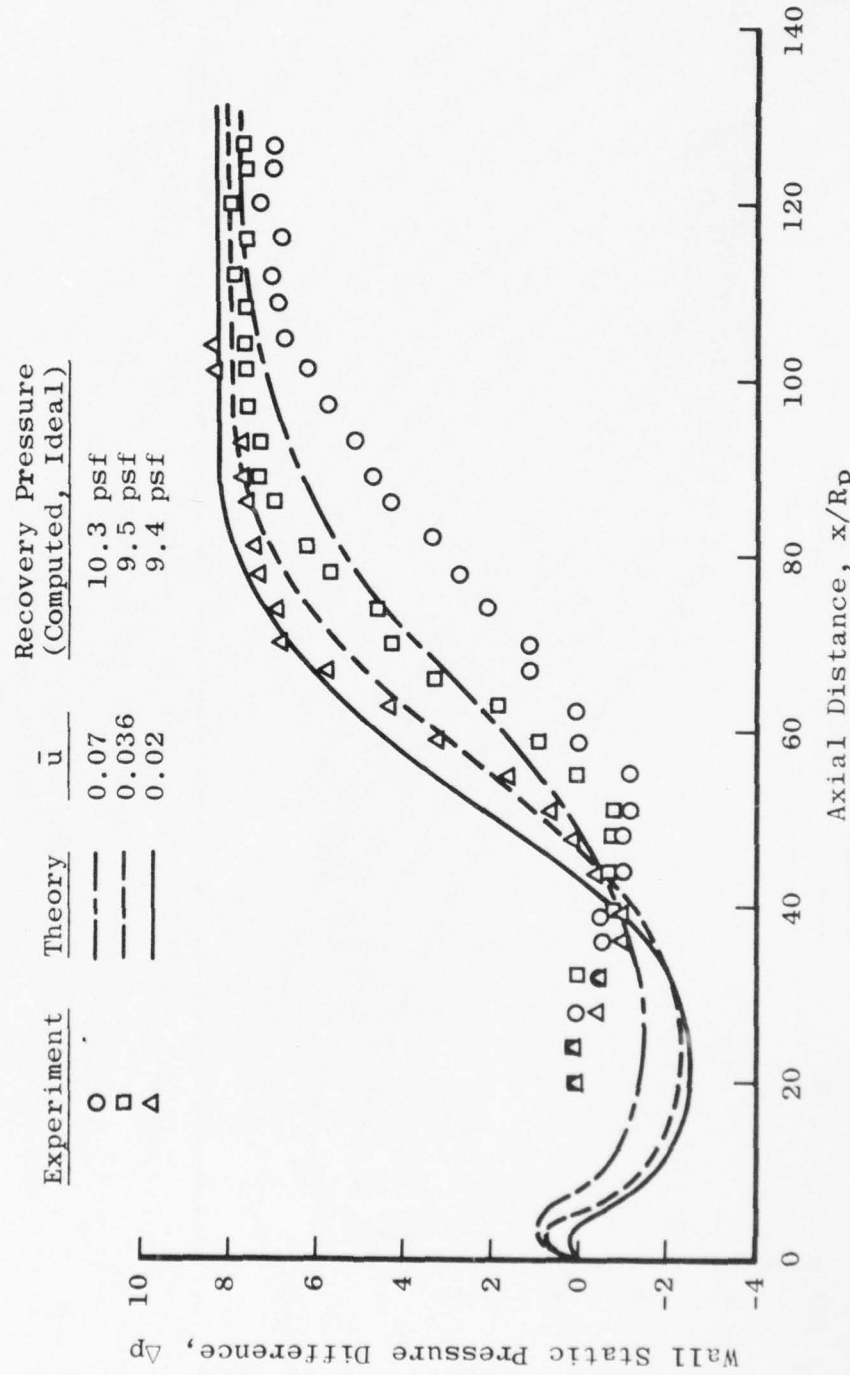


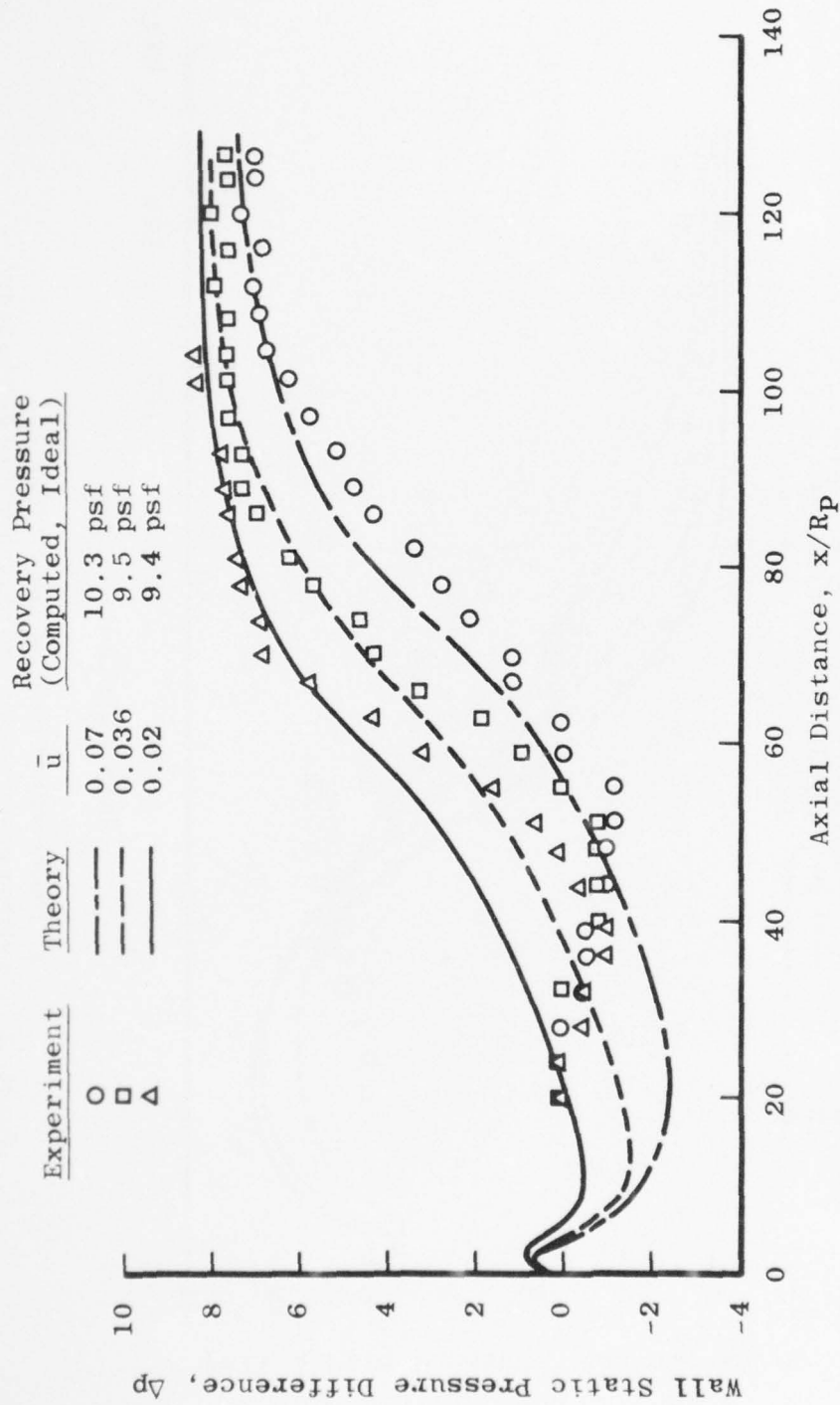
Figure 11. Continued.



c. $\bar{u} = 0.07$
Figure 11. Concluded.



a. Theory without potential cone modeling
Figure 12. Comparison of experimental and theoretical axial distributions
of wall static pressure.



b. Theory with potential cone modeling
Figure 12. Concluded.

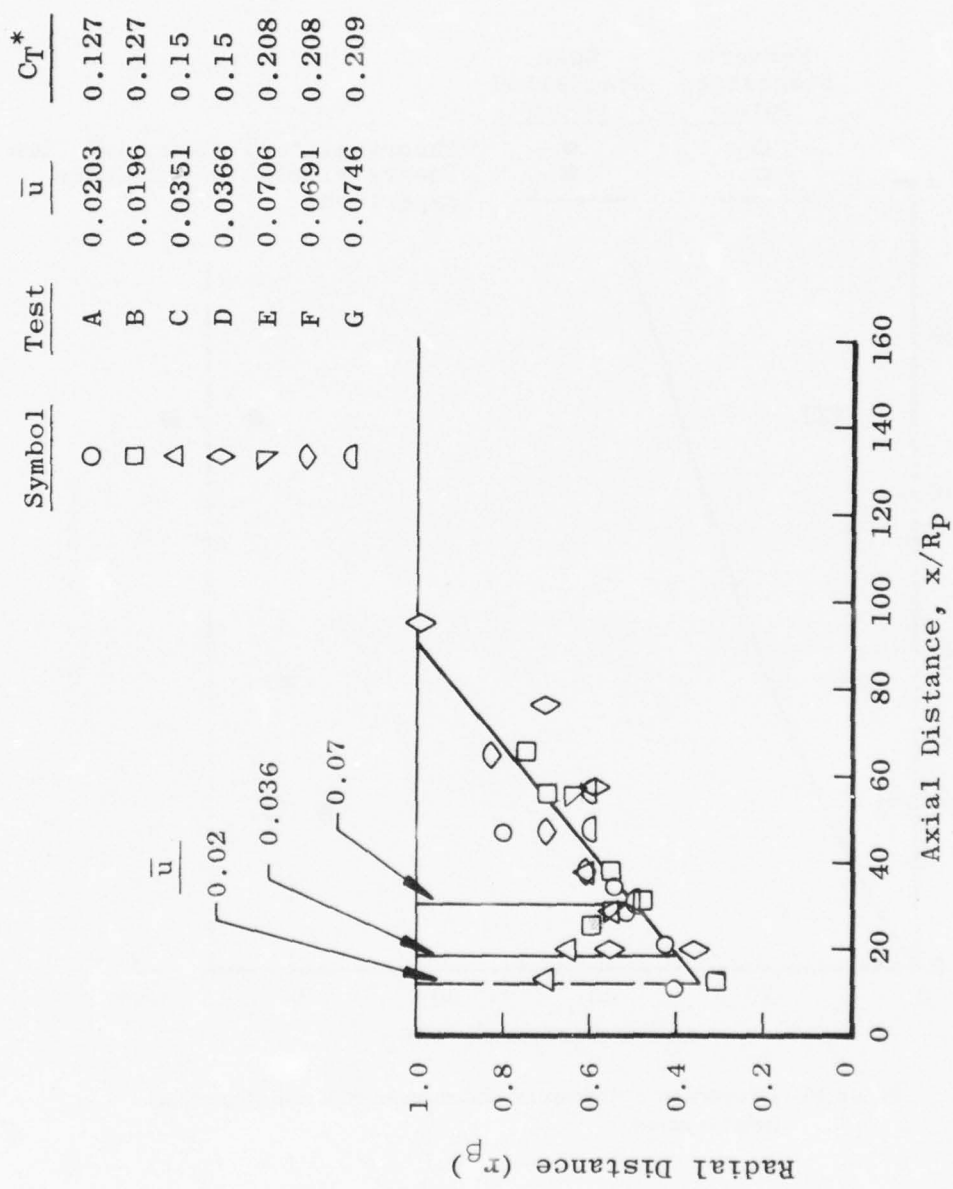


Figure 13. Estimated locations of points of zero mean axial velocity.

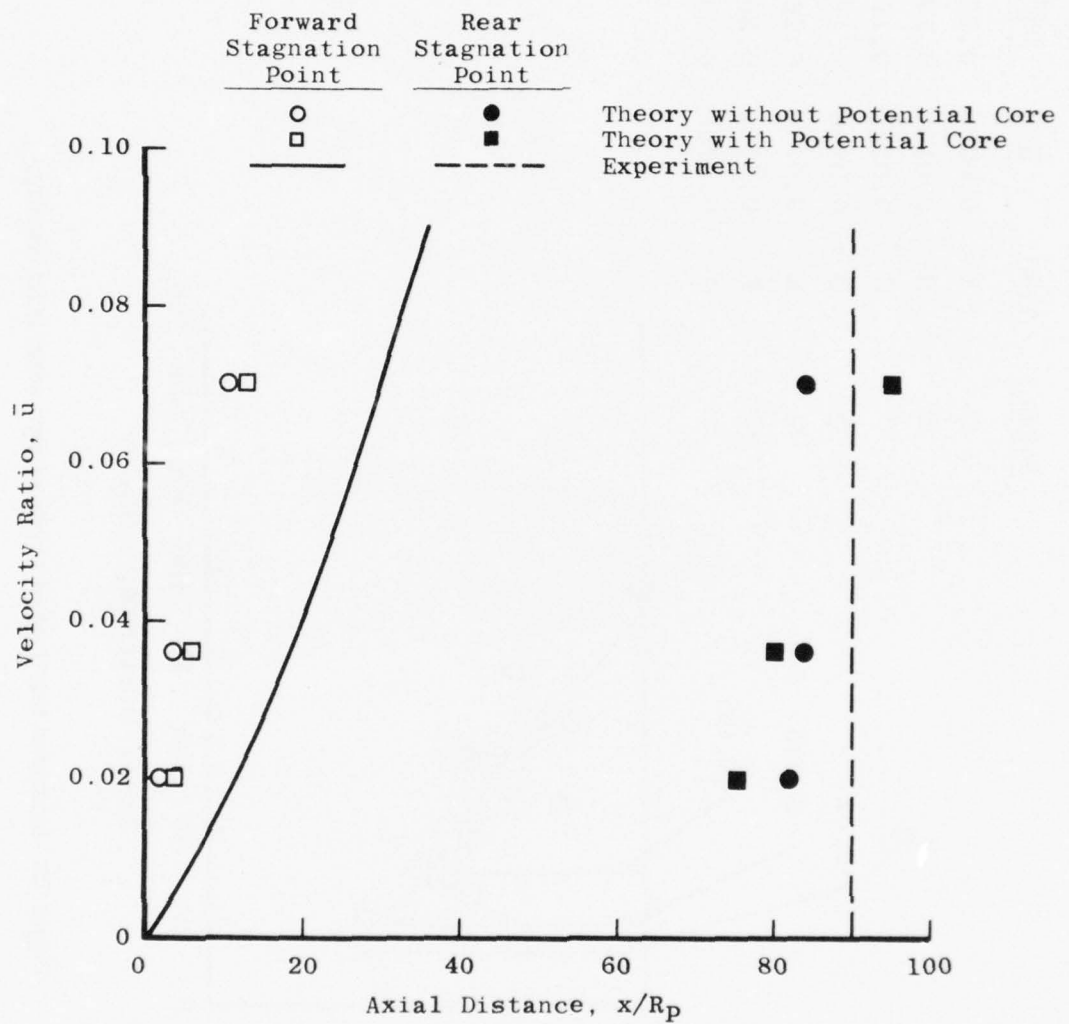


Figure 14. Comparison of theoretical and experimental wall stagnation point location.

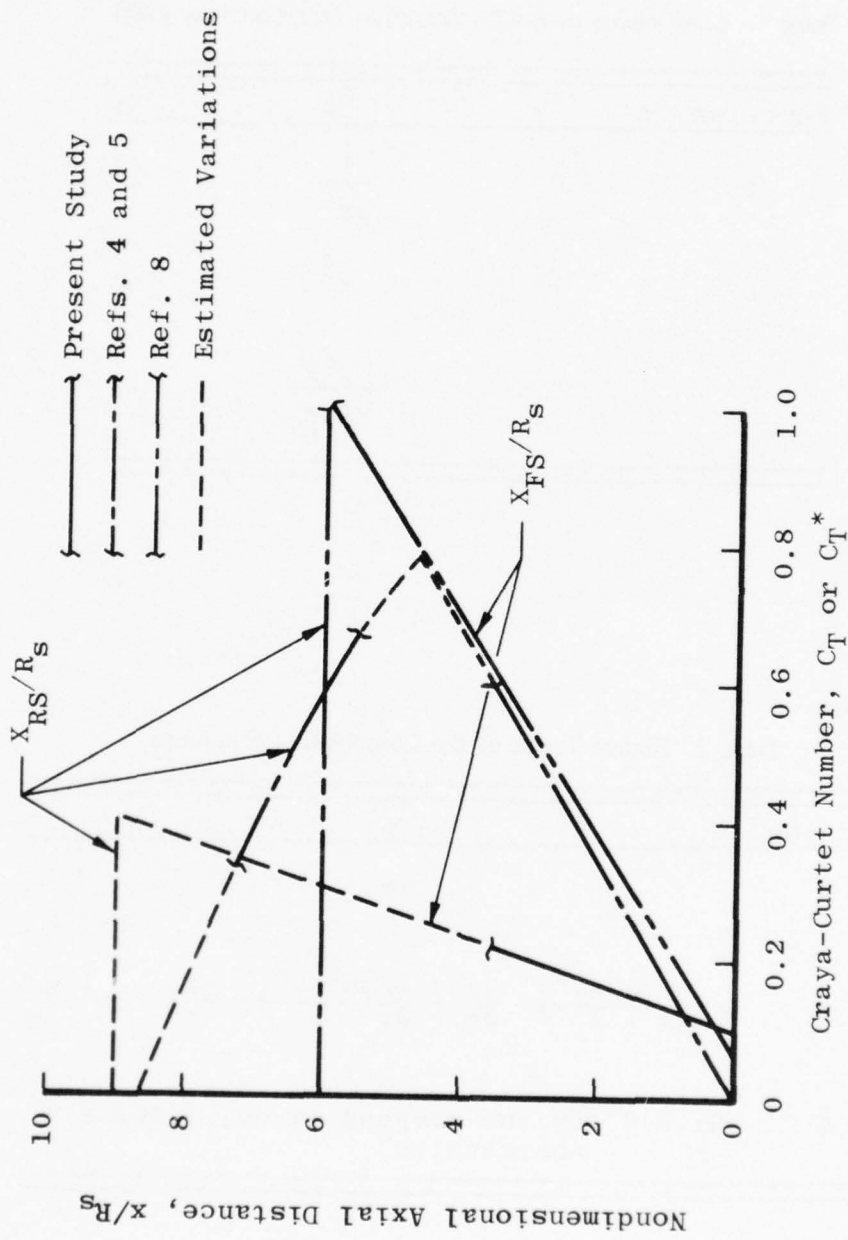


Figure 15. Axial locations of forward and rear stagnation points in recirculating combustor flows for constant and variable density jet mixing as functions of the Craya-Curlett number.

Table 1. Coefficients of the Conservation Equation (Eq. (12))

Function, ϕ	a_ϕ	b_ϕ	c_ϕ
ψ	0	$\frac{1}{\rho r^2}$	1
ω	r^2	r^2	μ_E
\tilde{C}	1	$\frac{\mu_E}{N_S c_{\tilde{C}}}$	1

Table 2. Source Terms of the Conservation Equations

Function	d_ϕ
ψ	$-\omega$
ω	$-r \left[\frac{\partial}{\partial x} \left(\frac{u^2 + v^2}{2} \right) \cdot \frac{\partial \rho}{\partial r} - \frac{\partial}{\partial r} \left(\frac{u^2 + v^2}{2} \right) \cdot \frac{\partial \rho}{\partial x} \right] - r^2 s_\omega$
\tilde{C}	$R_{\tilde{C}} \equiv 0$ (in the present study, flows are nonreactive)

Table 3. Uncertainties in Measured and Calculated Parameters (ϕ)

Parameter Name and Symbol, ϕ	Precision Index, S_ϕ , Percent of ϕ_R	Bias Limit, B_ϕ , Percent of ϕ_R	Uncertainty $U_\phi = \pm(B_\phi + t_{15} S_\phi)$, Percent of ϕ_R	Characteristic Value of ϕ for Establishing the Uncertainty, ϕ_R
Air Supply Total Pressure	± 1.0	± 3.0	± 5.0	250 psig
Hydrogen Supply Total Pressure	± 1.0	± 3.0	± 5.0	100 psig
Air Supply Total Temperature	± 0.15	± 1.8	± 2.1	530°R
Hydrogen Supply Total Temperature	± 0.15	± 1.8	± 2.1	530°R
Primary Nozzle Plenum Pressure	± 1.0	± 3.0	± 5.0	5 psig
Secondary Nozzle Plenum Pressure	± 2.0	± 6.0	± 10.0	1 psig
Primary Nozzle Throat Static Pressure	± 1.0	± 3.0	± 5.0	3 psig
Exhaust Duct Static Pressure	± 2.0	± 6.0	± 10.0	1 psig
Wall Static Pressure	± 3.8	± 3.8	± 11.4	0.47 psig
Probe Pitot Pressure, High Range	± 1.0	± 3.0	± 5.0	3 psig
Probe Pitot Pressure, Low Range	± 2.0	± 4.0	± 8.0	0.025 psig
Wall Static Pressure for Velocity Calculations	± 2.0	± 4.0	± 8.0	0.025 psig
Hydrogen Gas Concentrations, High Range	± 4.0	± 2.0	± 10.0	0.90
Hydrogen Gas Concentrations, Low Range	± 1.0	± 1.5	± 4.0	0.1
Velocity, u High Range at $C_C = 0.1$	± 0.7	± 1.9	± 3.3	550 ft/sec
Velocity, u Low Range at $C_C = 0.90$	± 6.9	± 14.1	± 27.9	80 ft/sec
Air Supply Mass Flow	± 1.6	± 3.5	± 6.7	0.07 lbm/sec
Hydrogen Supply Mass Flow	± 1.6	± 3.5	± 6.7	0.035 lbm/sec
Probe Radial Position	± 0.6	± 5.0	± 6.2	5 in.
Axial Distance between Probe Tip and Nozzle Assembly	± 0.2	± 1.0	± 1.4	50 in.

Table 4. Hydrogen-Air Mixing Experimental Test Conditions

Typical Test Cell and Supply Conditions:

Primary Jet Total Temperature = 530°R
 Primary Jet Total Pressure = 17.31 psia
 Secondary Jet Total Temperature = 530°R
 Secondary Jet Total Pressure = 13.80 to 13.84 psia
 Static Pressure Level at Probe Station = 13.8 psia

Specific Conditions for Each Test:

Test	Primary Jet Velocity, u_p ft/sec	Secondary Stream Entrance Velocity (a), ft/sec	Fully Mixed Hydrogen Gas Concentrations, C_{CFM}	Velocity Ratio, $\bar{u} = u_p/u_{S_0}$	Craya-Curtet Number, C_T^*
A	670	13.6	0.124	0.0203	0.127
B	680	13.3	0.12	0.0196	0.127
C	655	23	0.196	0.0351	0.15
D	655	24	0.203	0.0366	0.15
E	680	48	0.329	0.0706	0.208
F	680	47	0.325	0.0691	0.208
G	670	50	0.342	0.0746	0.209

(a) Secondary Stream Entrance Velocity Calculated with One-Dimensional Flow Assumption Based on Metered Secondary Mass Flow

APPENDIX A EXPERIMENTAL DATA

Appendix A contains a summary of the experimental data obtained in the present study. The data are the measurements of time-averaged axial velocity, hydrogen gas mass fraction in the interior of the duct and on the duct wall, and the wall static pressures for the primary and secondary influx conditions shown in Table 4.

Table A-1. Mean Axial Velocity Field Data
a. Mean Axial Velocity, u , ft/sec, from Test A

x/R_p	r/R_s									
	-0.11	0	0.11	0.22	0.33	0.44	0.55	0.66	0.77	0.85
3.8	490	671	396						10.0	
11.0	470	664	434	61.7					-8.0	-29
20.0	426	628	437	249.3				-12.96	-33.8	-32.2
29.1	365.5	553	397.2	309.9	124.3				-31.9	-45.9
34.8	410.8	448.9	355.2	310.4	189.0	81.7			-30.5	-46.2
47.2	344.4	375.7	380.5	289.8	172.0	105.7				-22.7
56.3	256.0	275.7	255.1	202.9	164.5	93.9				
171.7	22.9	22.2	20.5	21.0	20.4	22.5	22.2	21.2	20.5	20.9

b. Mean Axial Velocity, u , ft/sec, from Test B

x/R_p	r/R_s									
	-0.11	0	0.11	0.22	0.33	0.44	0.55	0.66	0.77	0.85
3.8	140	671	610							
12.9	374	605	550	214				-22	-33	-31
25.8	391	529	466	332	128			-25	-42	-49
31.0	386	502	473	342	180	35		-16	-45	-53
38.1	367	472	444	343	212	94			-35	-62
56.3	255	282	289	247	186	132	72			-24
65.4	191	188	193	174	142	114	72	24		
76.3	103	123	106	104	80	67	54			

c. Mean Axial Velocity, u , ft/sec, from Test C

x/R_p	r/R_s									
	-0.11	0	0.11	0.22	0.33	0.44	0.55	0.66	0.77	0.85
20	471	617	449	142	30			-28	-38	-36
38.2	403	528	456	338	100	37	12	7	-35	-54
57.2	364	416	373	157	113	65				-30
76.3	117	129	118	99	77	44				
95.4	53	51	51	44	40	29	20		5	
114.5	31	30	30	30	30	29	28	28	29	29
171.7	28	28	28	28	29	29	30	30	30	31

Table A-1. Concluded
d. Mean Axial Velocity, u , ft/sec, from Test D

x/R_p	r/R_s									
	-0.11	0	0.11	0.22	0.33	0.44	0.55	0.66	0.77	0.85
11.0	496	653	452	98	48	54	53		-22	-38
20.0	487	623	474	319	52	29	36	-33	-40	-40
29.1	481	573	521	396	187	33	0	-26	-47	-57
38.1	311	521	507	385	215	116			-41	-58

e. Mean Axial Velocity, u , ft/sec, from Test E

x/R_p	r/R_s									
	-0.11	0	0.11	0.22	0.33	0.44	0.55	0.66	0.77	0.85
11.0	518	677	421	85	74	78	55			
29.1	480	613	468	372	158	45	42	48	40	
38.1	496	565	487	405	234	82	34	27	-28	-38
171.7	63	64	65	64	67	68	67	67	66	65

f. Mean Axial Velocity, u , ft/sec, from Test F

x/R_p	r/R_s									
	-0.11	0	0.11	0.22	0.33	0.44	0.55	0.66	0.77	0.85
20.0	476	651	460	303	64	41	31	34	28	
29.1	472	605	466	379	157	29	9	27	12	24
38.1	476	553	474	403	231	84			-15	-34
47.2	486	518	488	411	261	127	34		-18	-41
56.3	492	522	487	406	265	152	22			-44
65.3	466	502	464	383	252	150				-9
95.4	230	240	227	191	146	86				

g. Mean Axial Velocity, u , ft/sec, from Test G

x/R_p	r/R_s									
	-0.11	0	0.11	0.22	0.33	0.44	0.55	0.66	0.77	0.85
3.8	581	658	339	80	88	82	84	120	81	30
13.8	505	650	445	145	74	82	75	63	40	39
25.8	471	621	470	320	115	62	56	55	44	41
31.0	473	597	474	342	167	59	-68	-80	-80	-72
47.2	471	512	471	396	254	110	32	-47	-74	-76
56.3	479	508	479	397	267	152	72	0	-56	-68
114.5	142	142	134	128	112	91	72	60	49	20

Table A-2. Mean Hydrogen Mass Fraction Data - Interior Field Data
a. Mean Hydrogen Mass Fraction, C_C , from Test A

x/R_p	r/R_s									
	-0.11	0	0.11	0.22	0.33	0.44	0.55	0.66	0.77	0.85
3.8	0.02	0	0.072	0.5	0.45	0.51	0.5	0.52	0.53	0.45
11.0	0.021	0	0.018	0.388	0.362	0.374	0.329	0.339	0.312	0.315
20.0	0.023	0.007	0.021	0.191	0.216	0.234	0.225	0.213	0.228	0.215
29.1	0.019	0.028	0.022	0.140	0.166	0.163	0.161	0.159	0.156	0.158
34.8	0.107	0.03	0.018	0.130	0.149	0.155	0.152	0.149	0.149	0.146
47.2	0.121	0.118	0.120	0.129	0.136	0.139	0.139	0.139	0.139	0.139
56.3	0.129	0.129	0.130	0.132	0.133	0.135	0.136	0.136	0.137	0.137
171.7	0.135	0.135	0.135	0.135	0.133	0.134	0.135	0.133	0.134	0.133

b. Mean Hydrogen Mass Fraction, C_C , from Test B

x/R_p	r/R_s									
	-0.11	0	0.11	0.22	0.33	0.44	0.55	0.66	0.77	0.85
3.8	0.524	0	0	0.543	0.493	0.480	0.558	0.574	0.519	0.428
12.9	0.141	0.001	0.006	0.313	0.372	0.372	0.369	0.357	0.359	0.325
25.8	0.106	0.016	0.019	0.140	0.214	0.211	0.218	0.218	0.207	0.204
31.0	0.107	0.034	0.047	0.129	0.187	0.186	0.184	0.184	0.182	0.179
38.1	0.115	0.078	0.084	0.128	0.162	0.173	0.167	0.164	0.164	0.160
56.3	0.137	0.135	0.135	0.137	0.141	0.144	0.147	0.148	0.148	0.147
65.4	0.141	0.140	0.140	0.141	0.142	0.143	0.144	0.145	0.146	0.146
76.3	0.143	0.143	0.143	0.143	0.142	0.144	0.144	0.143	0.146	0.144

c. Mean Hydrogen Mass Fraction, C_C , from Test C

x/R_p	r/R_s									
	-0.11	0	0.11	0.22	0.33	0.44	0.55	0.66	0.77	0.85
20	0.036	0.005	0.035	0.390	0.516	0.515	0.498	0.457	0.448	0.449
38.2	0.047	0.037	0.082	0.205	0.266	0.269	0.262	0.255	0.257	0.255
57.2	0.166	0.152	0.163	0.194	0.213	0.221	0.222	0.222	0.221	0.219
76.3	0.202	0.200	0.202	0.204	0.207	0.208	0.210	0.211	0.211	0.212
95.4	0.207	0.206	0.206	0.207	0.208	0.208	0.207	0.207	0.206	0.208
114.5	0.207	0.206	0.207	0.209	0.209	0.208	0.208	0.208	0.207	0.207
171.7	0.208	0.208	0.207	0.209	0.210	0.209	0.209	0.209	0.209	0.209

Table A-2. Concluded
d. Mean Hydrogen Mass Fraction, C_C , from Test D

x/R_p	r/R_s									
	-0.11	0	0.11	0.22	0.33	0.44	0.55	0.66	0.77	0.85
11.0	0.028	0	0.03	0.836	0.856	0.823	0.835	0.810	0.766	0.742
20.0	0.046	0.005	0.038	0.468	0.606	0.629	0.611	0.611	0.590	0.590
29.1	0.066	0.024	0.032	0.202	0.459	0.454	0.439	0.429	0.422	0.429
38.1		0.053	0.065	0.193	0.342	0.342	0.328	0.317	0.303	0.303

e. Mean Hydrogen Mass Fraction, C_C , from Test E

x/R_p	r/R_s									
	-0.11	0	0.11	0.22	0.33	0.44	0.55	0.66	0.77	0.85
11.0	0.021	0	0.036	0.99	1.0	1.0	1.0	1.0	1.0	1.0
29.1	0.052	0.015	0.056	0.420	0.823	0.922	0.938	0.906	0.892	0.886
38.1	0.077	0.029	0.084	0.344	0.656	0.712	0.735	0.698	0.692	0.709
171.7	0.344	0.347	0.345	0.343	0.343	0.342	0.340	0.344	0.342	0.343

f. Mean Hydrogen Mass Fraction, C_C , from Test F

x/R_p	r/R_s									
	-0.11	0	0.11	0.22	0.33	0.44	0.55	0.66	0.77	0.85
20.0	0.039	0.003	0.033	0.563	0.923	1.00	1.00	0.989	0.998	0.982
29.1	0.054	0.013	0.047	0.365	0.767	0.869	0.864	0.880	0.830	0.831
38.1	0.075	0.028	0.073	0.308	0.605	0.683	0.671	0.645	0.645	0.602
47.2	0.118	0.054	0.113	0.292	0.475	0.541	0.532	0.503	0.494	0.470
56.3	0.176	0.113	0.166	0.291	0.397	0.451	0.450	0.439	0.428	0.433
65.3	0.235	0.196	0.230	0.302	0.358	0.389	0.399	0.396	0.394	0.393
95.4	0.326	0.326	0.327	0.330	0.331	0.335	0.338	0.339	0.338	0.338

g. Mean Hydrogen Mass Fraction, C_C , from Test G

x/R_p	r/R_s									
	-0.11	0	0.11	0.22	0.33	0.44	0.55	0.66	0.77	0.85
3.8	0.016	0.000	0.166	0.990	0.983	0.991	0.990	0.979	0.963	0.774
13.8	0.036	0.001	0.046	0.864	0.994	0.992	0.977	0.978	0.974	0.792
25.8	0.049	0.013	0.055	0.445	0.889	0.969	0.976	0.961	0.946	0.779
31.0	0.060	0.022	0.065	0.363	0.779	0.898	0.902	0.930	0.879	0.738
47.2	0.108	0.058	0.112	0.292	0.509	0.502	0.580	0.559	0.527	0.455
56.3	0.162	0.111	0.163	0.296	0.424	0.486	0.493	0.474	0.452	0.392
114.5	0.382	0.382	0.382	0.381	0.382	0.384	0.385	0.387	0.390	0.403

Table A-3. Hydrogen Mass Fraction at the Wall

Axial Distance, x/R_p	Test A	Test B	Test C	Test D	Test E	Test G
0						
1.43	0.371	0.334	0.683	0.624	0.772	0.986
5.25	0.383	0.332	0.713	0.646	1.00	---
9.07	0.272	---	0.581	0.552	1.00	0.872
12.88	0.272	0.269	0.502	0.518	1.00	0.958
16.70	0.237	0.244	0.494	---	0.700	0.907
20.52	0.207	0.201	0.417	0.442	0.993	0.742
24.33	0.186	0.187	0.383	0.389	1.00	---
28.15	0.169	0.188	0.346	0.326	0.937	0.763
31.97	0.159	0.156	0.314	0.306	0.832	0.698
35.78	0.159	0.141	0.273	0.275	0.811	0.655
39.60	0.149	0.137	0.256	0.267	0.564	0.627
43.42	0.143	0.145	0.239	0.245	0.569	---
47.23	0.135	0.126	0.228	0.225	0.535	0.496
51.05	0.135	0.128	0.241	0.239	0.463	0.462
54.87	0.143	0.115	0.220	0.225	0.486	0.444
58.68	0.139	0.130	0.217	0.228	0.405	0.465
62.50	0.136	0.134	0.216	0.223	0.444	---
66.32	0.130	0.137	0.206	0.208	0.417	0.409
70.13	0.130	0.131	0.209	0.207	0.373	0.399
73.95	0.146	0.132	0.204	0.211	0.415	0.409
77.77	0.133	0.128	0.204	0.225	0.323	0.411
81.58	0.132	0.133	0.200	0.211	0.374	---
85.40	0.126	0.137	0.197	0.200	0.357	0.363
89.22	0.128	0.126	0.202	0.207	0.340	0.358
93.03	0.137	0.131	0.198	0.207	0.340	0.357
96.85	0.134	0.126	0.199	0.215	0.335	0.095
100.67	0.143	0.141	0.215	0.222	0.380	---
104.49	0.127	0.140	0.196	0.199	0.344	0.333
108.30	0.129	0.127	0.202	0.204	0.329	0.345
112.12	0.138	0.130	0.199	0.203	0.333	0.326
115.94	0.135	0.128	0.204	0.214	0.340	0.366
119.75	0.135	0.137	0.203	0.206	0.364	---
120.71						0.324
121.66						

Table A-4. Wall Static Pressure Distributions

Axial Distance, x/R_p	Δp , psf		
	$\bar{u} = 0.02$	$\bar{u} = 0.036$	$\bar{u} = 0.07$
0	0	0	0
1.43	0	0	0
5.25	0	0	0
9.07	0	0	0
12.88	0	0	0
16.70	0	0	0
20.52	0	0	0
24.33	0	0	0
28.15	-0.55	0	0
31.97	-0.55	0	-0.53
35.78	-1.00	-0.57	-0.53
39.60	-1.00	-0.80	-0.53
43.42	-0.55	-0.80	-1.05
47.23	0	-0.80	-1.05
51.05	-0.55	-0.80	-1.05
54.87	1.55	0	-1.05
58.68	3.10	0.85	0
62.50	4.15	1.841	0
66.32	5.70	3.31	1.05
70.13	6.75	4.34	1.05
73.95	6.75	4.63	2.10
77.77	7.30	5.67	2.63
81.58	7.76	6.19	3.33
85.40	7.76	6.99	4.16
89.22	7.76	7.32	4.64
93.03	7.76	7.32	5.21
96.85	7.76	7.56	5.69
100.67	8.26	7.74	6.21
104.49	8.26	7.74	6.78
108.30	7.76	7.74	6.78
112.12	7.76	8.03	7.00
115.94	7.76	7.56	6.78
120.71	8.26	8.03	7.31
123.56	7.76	7.56	7.00
127.39	7.76	7.56	7.00
131.20	7.76	7.56	6.74

NOMENCLATURE

A	Area
B_ϕ	Bias of the parameter (ϕ), units of ϕ
C_c	Hydrogen gas mass fraction
C_T	Craya-Curtet number, (Eq. (2))
C_T^*	Variable density Craya-Curtet number (Eq. (39))
\tilde{C}	Transported scalar quantity
$D_{\tilde{C}_E}$	Effective diffusion coefficient, ft^2/sec
d_ϕ	Source term (Eq. (12))
L	Length, ft or in. as noted
l_t	Thickness of primary nozzle lip in the theoretical solution procedure (Fig. 2)
N_{Re}	Reynolds number, $N_{Re} = \rho u L / \mu$
$N_{Sc\tilde{C}}$	Effective Schmidt number, $N_{Sc} = \mu_E / \rho D_{\tilde{C}_E}$
p_t	Total pressure, psfa
p	Static pressure, psfa

Δp	Wall static pressure difference defined as the wall static pressure at a given axial distance from the primary nozzle exit plane minus the wall static pressure in the primary nozzle exit plane, $\Delta p = p(x) - p(o)$, psfa
R_N	Radius to nodal point in the theoretical solution procedure
R_p	Primary nozzle radius, ft or in. as noted
R_s	Duct radius, ft or in. as noted
R_{p1}	Radius of primary nozzle outer lip in the theoretical solution procedure (Fig. 2)
r	Radial coordinate
r_β	Nondimensional radial coordinate, $r_\beta = r/R_s$
S_ϕ	Precision index of the parameter (ϕ), units of ϕ
T_t	Total temperature, °R
u	Time-averaged axial velocity, ft/sec
u_m	Maximum axial velocity, also, axial velocity on the centerline of the duct, ft/sec
\bar{u}	Velocity ratio, $\bar{u} = u_p/u_{s_o}$
u_p	Velocity of jet from primary nozzle, ft/sec
u_s	Secondary stream velocity at given axial station, ft/sec

u_{s_0}	Secondary stream velocity at primary nozzle exit plane, ft/sec
u_k	Characteristic velocity for confined jet mixing, ft/sec (Eq. (3))
u_o^*	Characteristic velocity for confined jet mixing, ft/sec (Eq. (4))
u_k^*	Characteristic velocity for variable density confined jet mixing, ft/sec (Eq. (42))
u_o^{**}	Characteristic velocity for variable density confined jet mixing ft/sec (Eq. (43))
U_ϕ	Uncertainty in the parameter (ϕ), units of ϕ
v	Time-averaged radial velocity, ft/sec
x_{core}	Length of velocity potential core, $12 R_p$ in present theoretical study
x_{FS}	Axial distance between the primary nozzle exit plane and the forward stagnation point on the duct wall (Fig. 1)
x_{RS}	Axial distance between the primary nozzle exit plane and the rear stagnation point on the duct wall (Fig. 1)
x_α	Nondimensional axial coordinate, x/R_p
x	Axial coordinate
λ	Coefficient in the definition of corner vorticity (Eq. (25))
μ	Dynamic viscosity, lbm/ft-sec
μ_E	Effective dynamic viscosity, lbm/ft-sec

ρ	Density, lbm/ft^3
ρ_k^*	Characteristic density for variable density confined jet mixing (Eq. (44))
ρ_o^*	Characteristic density for variable density confined jet mixing, (Eq. (45))
ϕ	Dummy parameter, scalar
ψ	Stream function (Eqs. (8) and (9))
Ω	Vorticity (Eq. (11))
ω	Vorticity divided by radius, Ω/r

SUBSCRIPTS

CA	Primary nozzle lower lip corner point (Fig. 2)
CB	Primary nozzle upper lip corner point (Fig. 2)
D	Diameter
E	Effective or "Eastern"
LAM	Molecular property
N	Nodal or "Northern"
o	Zero axial station
p	Primary jet property

AEDC-TR-76-152

S "Southern" or secondary stream property

W Wall or "Western"